Materials Science and Engineering B 320 (2025) 118410

Contents lists available at ScienceDirect

Materials Science & Engineering B

journal homepage: www.elsevier.com/locate/mseb

Unveiling the photocatalytic activities of morphology-controlled ZrO_2, BaO, and Y_2O_3 nanoparticles using *Eucalyptus* leaf extract

Pushpa Mani [a], Mageswari Subramanian [b,*], Panneerselvam Arputham [a]

[a] Department of Physics, Vivekanandha College of Engineering for Women Elayampalayam, Tiruchengode 637205 Tamil Nadu, India
[b] Department of Chemistry, Vivekanandha College of Engineering for Women Elayampalayam, Tiruchengode 637205 Tamil Nadu, India

ARTICLE INFO

Keywords:
Transition metal oxide nanoparticles
Green synthesis
Barium oxide nanoparticles
Photocatalytic activity

ABSTRACT

This study investigates the synthesis of transition metal oxide nanoparticles, including Zirconium oxide (ZrO_2), Barium oxide (BaO), and Yttrium oxide (Y_2O_3), using *Eucalyptus* leaf extract as a green reducing agent through a sonication-assisted approach. The nanoparticles were thoroughly characterized for their crystalline structure, functional groups, morphology, and elemental composition. The results confirmed the successful formation of distinct metal oxide bonds and unique morphological features: ZrO_2 exhibited semi-spherical shapes, BaO showed monodisperse spherical morphology, and Y_2O_3 displayed a flaky non-spherical structure. The photocatalytic activity of the nanoparticles was evaluated for the degradation of Brilliant Blue (BB) and Rhodamine B (RhB) dyes. Among the samples, BaO nanoparticles achieved the highest degradation efficiency, reaching up to 99 % for both dyes under natural sunlight. Antibacterial studies revealed significant activity, with BaO exhibiting 18 mm and 21 mm inhibition zones against *E. coli* and *S. aureus*. Real-time turbidimetric growth inhibition tests further demonstrated BaO's superior performance, with growth inhibition rates of 81.4 % and 88.6 % against *E. coli* and *S. aureus*. Additionally, antioxidant activity assessed through the DPPH assay indicated that BaO nanoparticles exhibited the highest radical scavenging ability, surpassing ZrO_2 and Y_2O_3. These findings underscore the multifunctional capabilities of BaO nanoparticles, particularly in environmental remediation applications such as dye degradation, antibacterial treatments, and antioxidant activity, highlighting their potential for sustainable and eco-friendly solutions to pressing biological and ecological challenges.

1. Introduction

The textile dyeing industry has a history of 4,000 years, with natural dyes dominating until synthetic dyes emerged 150 years ago. Today, many dyes are used in textiles, leather, and printing to colour materials like fabrics, carpets, and inks. Approximately 7 million tons of textile dyes are produced annually, with around 10 % discharged into water bodies as industrial effluent [1,2]. Among these, the most prominent are azo, anthraquinone, and phthalocyanine dyes. Azo dyes account for over 1 million tons of annual production and are widely used in textiles, printing, pharmaceuticals, cosmetics, and food processing [3,4]. Azo dyes are classified as micropollutants due to their persistence in aquatic environments, even at low concentrations (ng/L). Their presence disrupts sunlight penetration, affecting photosynthesis and biological activity in marine ecosystems while reducing dissolved oxygen levels [5]. These dyes contribute significantly to coloured wastewater, with dye wastage in the textile industry ranging from 5 % to 50 %, resulting in approximately 200 billion litres of effluent annually. Slow or negligible biodegradation further exacerbates their environmental impact, leading to prolonged contamination. Azo and anthraquinone dyes are toxic to aquatic life, affecting bacteria, microalgae, and ciliates, and pose health risks to humans, including mutagenic effects and kidney diseases [6,7]. Therefore, removing these dyes from industrial effluents is essential to mitigate environmental and biological hazards.

Various techniques have been explored to eliminate harmful dye contaminants, including adsorption, coagulation, flocculation, membrane filtration, ion exchange, and ozonation [8–12]. However, these methods often merely transform the dye components into different states, leaving their toxic nature largely unchanged. Consequently, current research efforts are focused on removing dye pollutants and their degradation into non-toxic byproducts. Among the available approaches, photocatalytic degradation has emerged as a highly effective technique for achieving this dual goal. The photocatalytic degradation technique employs a photocatalyst material to mineralize organic

* Corresponding author.
E-mail address: mmahes15@gmail.com (Mageswari Subramanian).

https://doi.org/10.1016/j.mseb.2025.118410
Received 3 March 2025; Received in revised form 30 April 2025; Accepted 8 May 2025
0921-5107/© 2025 Elsevier B.V. All rights are reserved, including those for text and data mining, AI training, and similar technologies.

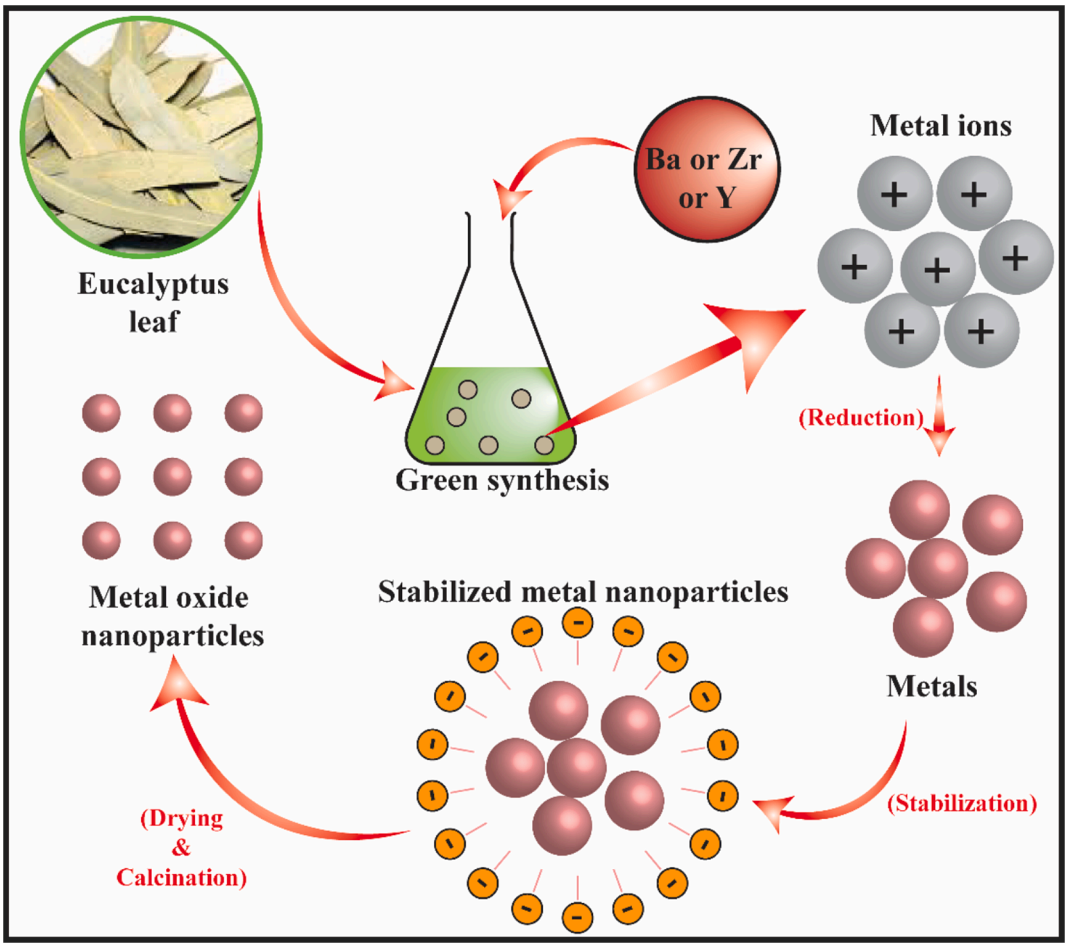


Fig. 1. A brief representation of the synthesis of ZrO_2, BaO, and Y_2O_3 samples.

pollutants effectively in contaminated water into harmless byproducts such as carbon dioxide and water [13–15]. The photocatalytic degradation efficiency depends on the properties of the photocatalyst materials, which should possess an optimal band gap energy, prolonged charge carrier recombination time, high photoactivity, superior adsorption capacity, and robust chemical stability. Transition metal oxide nanoparticles are up-and-coming candidates, exhibiting these desirable characteristics. A variety of such nanoparticles, including titanium oxide (TiO_2), zinc oxide (ZnO), cobalt oxide (Co_3O_4), nickel oxide (NiO), and tin oxide (SnO_2), have been extensively studied for their efficacy in degrading dye pollutants through photocatalytic processes [16–19].

Several transition metal oxide nanoparticles have been comparatively less studied but offer significant advantages as photocatalysts. Zirconium oxide (ZrO_2) nanoparticles stand out due to their exceptional optical and electronic properties. Their notably low conduction band energy and wide band gap facilitate the efficient generation of oxygen vacancies, which act as active sites for catalytic interactions [20,21]. Combined with their remarkable stability, these properties render ZrO_2 nanoparticles highly effective as photocatalysts. Similarly, barium oxide (BaO), an alkaline earth metal oxide family member, demonstrates exceptional catalytic activity, particularly in the epoxidation of terminal alkenes such as styrene [22–24]. The high stability and distinctive properties of BaO nanoparticles reduce the reliance on conventional transition metal oxide (TMO) photocatalysts, which are often prone to corrosion. Another rare earth metal oxide nanoparticle with significant potential as a photocatalyst, though relatively underexplored, is yttrium oxide (Y_2O_3). Y_2O_3 nanoparticles exhibit a wide optical band gap and excellent chemical and thermal stability [25–27]. Beyond photocatalysis, they are also recognized as key components in the fabrication of optoelectronic devices, highlighting their versatility and importance in advanced materials research.

This study adopts a novel approach to synthesizing the transition metal oxide nanoparticles, namely ZrO_2, BaO, and Y_2O_3. It investigates their potential multifaceted applications in dye pollutant degradation, antioxidant activity, and antibacterial properties. A green synthesis methodology was employed to ensure an environmentally sustainable synthesis process, utilizing *Eucalyptus leaf* extract as a natural reducing agent. Specifically for photocatalytic degradation of organic pollutants, green synthesis of nanoparticles offers several advantages, including environmental friendliness, cost-effectiveness, and enhanced biocompatibility. *Eucalyptus*, a genus belonging to the *Myrtaceae* family, is widely recognized for its rapid growth and adaptability to diverse climatic conditions [28]. Phytochemical analyses of *Eucalyptus* leaves reveal an abundance of bioactive compounds, such as flavonoids, tannins, terpenoids, and essential oils. These phytochemicals are crucial in reducing metal salts to nanoparticles while imparting the synthesized materials with potent antibacterial and antifungal properties [29]. Traditionally, *Eucalyptus* has been employed in herbal medicine to treat ailments like respiratory infections, arthritis, and skin conditions. *Eucalyptus* extracts are known for their effectiveness as natural disinfectants and insect repellents [30]. The bioactive components of *Eucalyptus* not only serve as reducing agents in nanoparticle synthesis but also enhance the functional properties of nanomaterials, making them highly effective in applications like photocatalytic degradation and microbial inhibition.

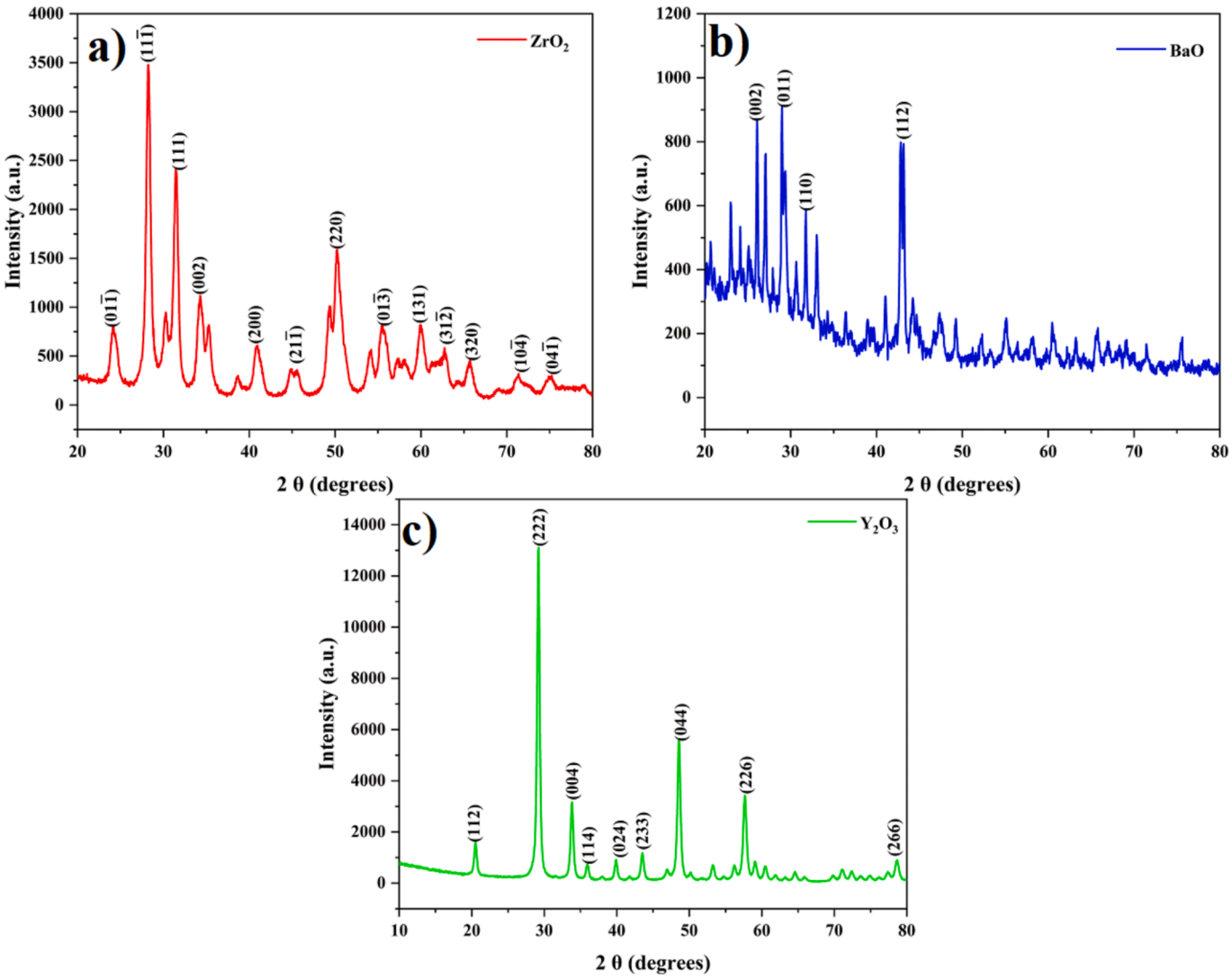


Fig. 2. XRD spectra of prepared a) ZrO_2, b) BaO and c) Y_2O_3.

2. Experimental procedure

2.1. Materials required

The precursor metal salts used in this study are Barium chloride dihydrate ($BaCl_2{\cdot}2H_2O$) (99 % purity), Zirconium Oxychloride Octahydrate ($ZrO_2Cl_2{\cdot}8H_2O$) (99.5 % purity), and Yttrium (III) Chloride Hexahydrate extra pure ($YCl_3{\cdot}6H_2O$) (99.9 % purity). The *Eucalyptus* leaf was used as a reducing and capping agent and was acquired from local forms near Tiruchengode, Tamilnadu, India. This study used absolute ethanol and double-distilled (DD) water as solvents. The chemicals and solvents used in this study were purchased from Loba Chemie., India.

2.2. Preparation of Eucalyptus leaf extract

The collected *Eucalyptus* leaves were washed several times with DD water and shade-dried for 3 days to remove moisture. The leaves were then fine-grounded with a domestic mixer and stored in a desiccator. 30 g of *Eucalyptus* leaf powder was then dispersed into 300 mL of DD water and boiled for 6 h at 80 °C. The extract was then centrifuged at 7000 rpm to collect the supernatant. The supernatant was again filtered with Whatman No. 1 filter paper to remove smaller constituents. The purified extract was then split into 100 mL to synthesize ZrO_2, BaO, and Y_3O_4 nanoparticles.

2.3. Preparation of ZrO_2, BaO and Y_3O_4 nanoparticles

The synthesis of ZrO_2 nanoparticles was carried out using a green synthesis approach facilitated by *Eucalyptus* leaf extract. Initially, 0.1 M of zirconium oxychloride octahydrate was dissolved in 100 mL of freshly prepared *Eucalyptus* leaf extract under constant stirring to achieve complete homogeneity. After the reaction, the solution was allowed to cool to room temperature and was then subjected to ultrasonication for 120 min using a probe sonicator (operating at 10 s work time and 5 s rest intervals). This process ensured uniform nucleation and dispersion of nanoparticles. The sonicated solution was left undisturbed at room temperature for 24 h to allow homogeneous nucleation and particle growth. The resultant solution was centrifuged at 6000 rpm for 15 min to collect the formed nanoparticle pellet. The pellet was thoroughly washed multiple times with 70 % ethanol and deionized water to remove unreacted precursors or residual impurities. The washed pellet was dried in a hot air oven at 70 °C for 6 h. The dried material was ground into a fine powder using a mortar and pestle and subsequently calcined at 500 °C for 2 h in a muffle furnace to enhance the crystallinity of the nanoparticles. A similar synthesis protocol was followed to prepare barium oxide (BaO) and yttrium oxide (Y_2O_3) nanoparticles. For these, zirconium oxychloride was replaced with barium chloride

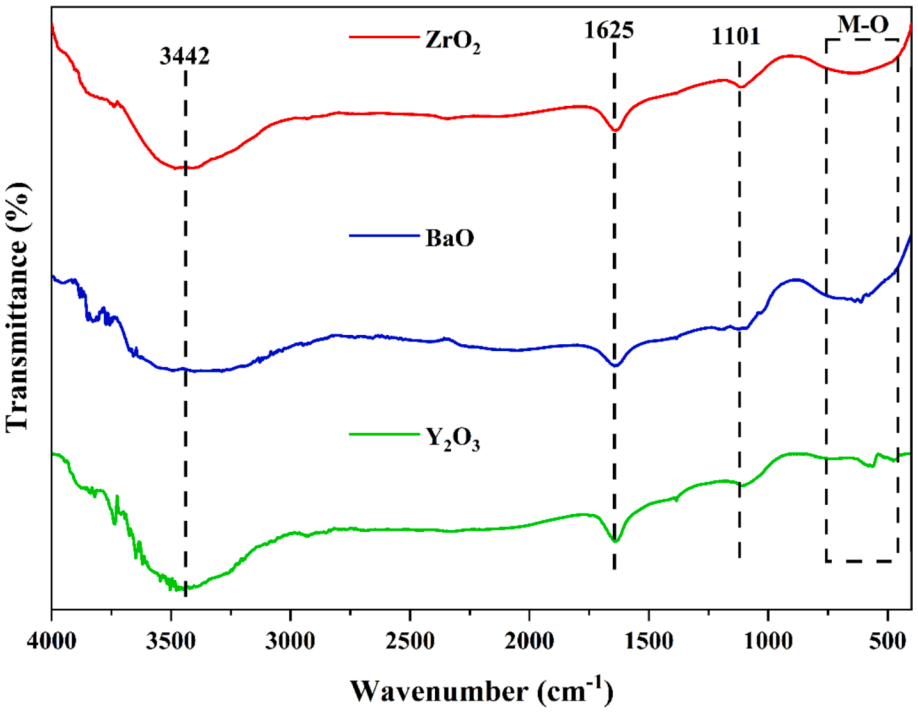


Fig. 3. FTIR spectrum of prepared metal oxide nanoparticles with *Eucalyptus leaf* extract.

dihydrate and yttrium (III) chloride hexahydrate, respectively, in the same stoichiometric concentration. The synthesized zirconium, barium, and yttrium oxide nanoparticles were designated ZrO2, BaO, and Y2O3 for further characterization and studies. A brief graphical representation of the synthesis procedure is depicted in Fig. 1. The yield of obtained ZrO_2, BaO, and Y_2O_3 nanoparticles from the performed methodology is 61.41 %, 49.53 %, and 38.46 %, respectively.

2.4. Characterization techniques

The crystalline properties of prepared ZrO_2, BaO, and Y_2O_3 nanoparticles were examined using X-ray diffraction analysis (Bruker D2-Phaser). The functional group attachments and role of *Eucalyptus* leaf as an effective reducing agent were evaluated with functional group analysis utilizing Fourier transform infrared spectroscopy (FTIR) (PerkinElmer spectrum two FTIR spectrometer). The surface morphological analysis was carried out using a Field emission scanning electron microscope fitted with an Energy dispersive x-ray analysis to evaluate the elemental composition of the prepared Transition metal oxide nanoparticles (SIGMA HV – Carl Zeiss with Bruker Quantax 200 – Z10 EDS Detector). The optical absorbance of prepared samples was analyzed using UV–Vis spectroscopy (UV–Vis) (JASCO V-750 SPECTROPHOTOMETER). The particle size of the prepared samples was analyzed using a Particle size analyzer (PSA) (Anton Paar, Litesizer 500).

2.5. Antibacterial examination

Fresh cultures of *Escherichia coli (E. coli*) and *Staphylococcus aureus (S. aureus)* were prepared by inoculating a single bacterial colony from each strain into separate nutrient broth media. These cultures were incubated at 37 °C for 18–24 h to ensure sufficient bacterial growth. Following incubation, the bacterial suspensions were standardized to match the turbidity of a 0.5 McFarland standard, ensuring uniformity in bacterial concentration. Mueller-Hinton agar plates were then prepared, and the standardized bacterial suspensions were evenly spread across the surface using sterile cotton swabs to ensure uniform inoculation. In each agar plate, wells with a diameter of 6 mm were carefully created using a sterile borer. Into these wells, 50 μL of nanoparticle solutions, specifically ZrO_2, BaO, and Y_2O_3, were introduced at varying concentrations of 25, 50, 75, and 100 μg/mL. A commercially available antimicrobial agent (S25) was included as a positive control to provide a reference for bacterial inhibition, while a well containing only the solvent served as a negative control to validate the test system. The agar plates were incubated at 37 °C for 24 h to allow the nanoparticles to interact with the bacterial strains. After incubation, the zones of inhibition around the wells were measured using a vernier calliper to determine the antibacterial efficacy of the nanoparticles.

2.6. Bacterial growth reduction analysis (turbidimetric analysis)

The antibacterial efficacy of the synthesized nanoparticles was evaluated using a turbidometric assay by measuring the inhibition of bacterial growth over time. Fresh cultures of *E. coli and S. aureus* were grown in nutrient broth and standardized to match the turbidity of a 0.5 McFarland standard. In sterilized test tubes, 2 mL of the bacterial suspension was combined with 1 mL of nanoparticle solutions at 25, 50, 75, and 100 μg/mL concentrations. A control tube containing 2 mL of bacterial suspension and 1 mL of sterile distilled water was prepared for comparison. A blank solution consisting of nutrient broth without bacteria or nanoparticles was also included to serve as a reference for spectrophotometer calibration. The test tubes were incubated at 37 °C, and the samples' optical density (OD) was measured at 600 nm using a UV–Vis spectrophotometer at intervals of 60 min for a total duration of 360 min. The extent of bacterial growth inhibition was determined using the following formula [31]:

$$\text{Growth inhibition efficiency} = \frac{\text{OD of control} - \text{OD of test}}{\text{OD of control}} \times 100$$

2.7. Free radical scavenging activity

The antioxidant activity of the synthesized ZrO_2, BaO, and Y_2O_3 nanoparticles was determined using the DPPH (2,2-diphenyl-1-picrylhydrazyl) radical scavenging assay. Stock solutions of the nanoparticles were prepared by dispersing them in methanol (100 %) to

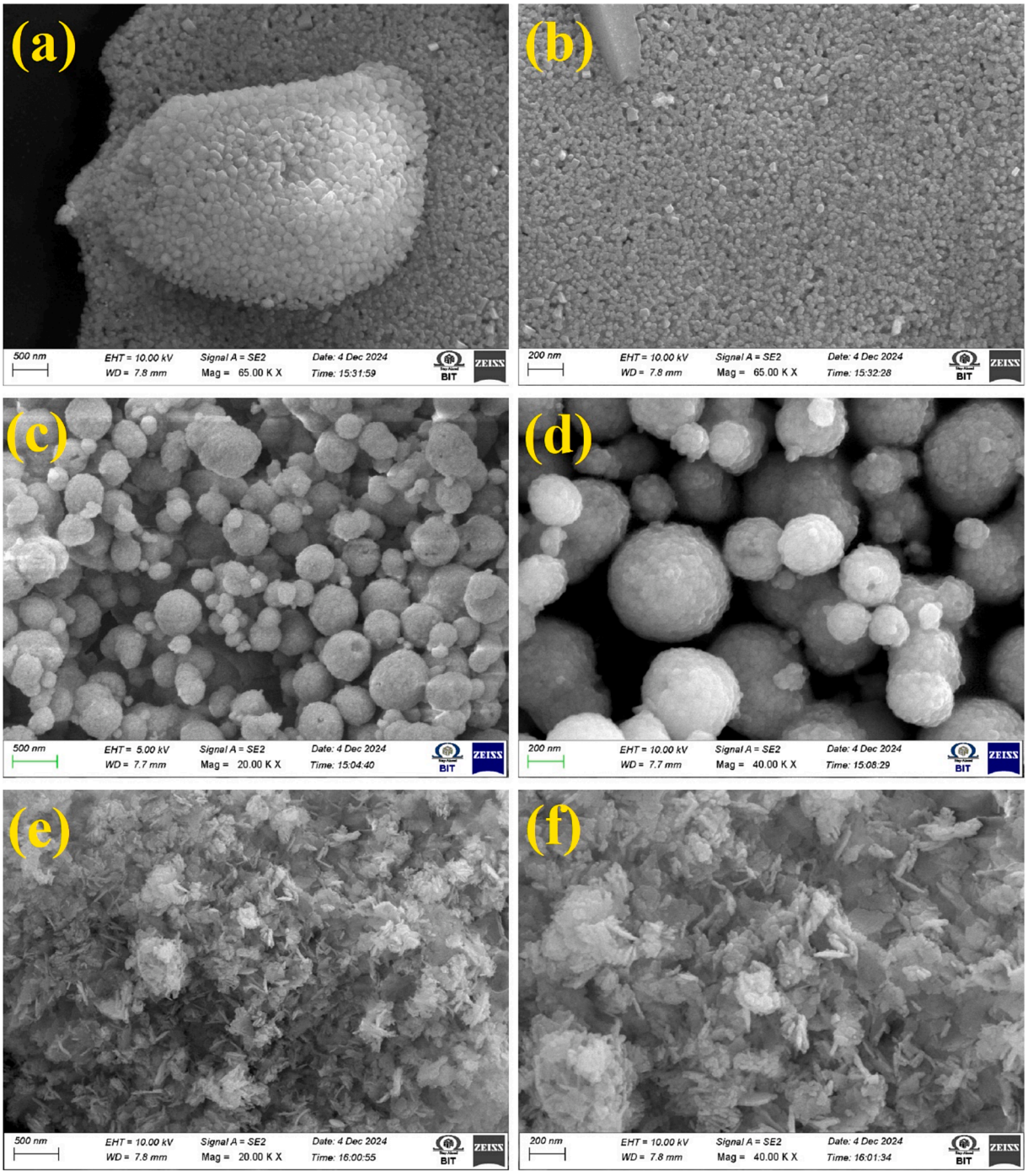


Fig. 4. Surface morphology analysis of prepared ZrO_2 (a-b), Bao (c-d) and Y_2O_3 (e-f).

achieve various concentrations (25, 50, 75, and 100 μg/mL). A DPPH solution was prepared by dissolving 0.1 mM DPPH in methanol and shielding it from light to maintain stability. For the assay, 2 mL of the DPPH solution was mixed with 1 mL of the nanoparticle solution in clean test tubes. The methanol solution was used as a blank in the scavenging activity. All test tubes were incubated in the dark at room temperature for 30 min to allow the reaction to occur. After incubation, the absorbance of the reaction mixtures was measured at 517 nm using a UV–Vis spectrophotometer. The percentage of DPPH radical scavenging activity was calculated using the following formula [32]:

$$\text{Radical scavenging activity}\ (\%) = \frac{\text{Absorbance of control} - \text{Absorbance of sample}}{\text{absorbance of control}}$$

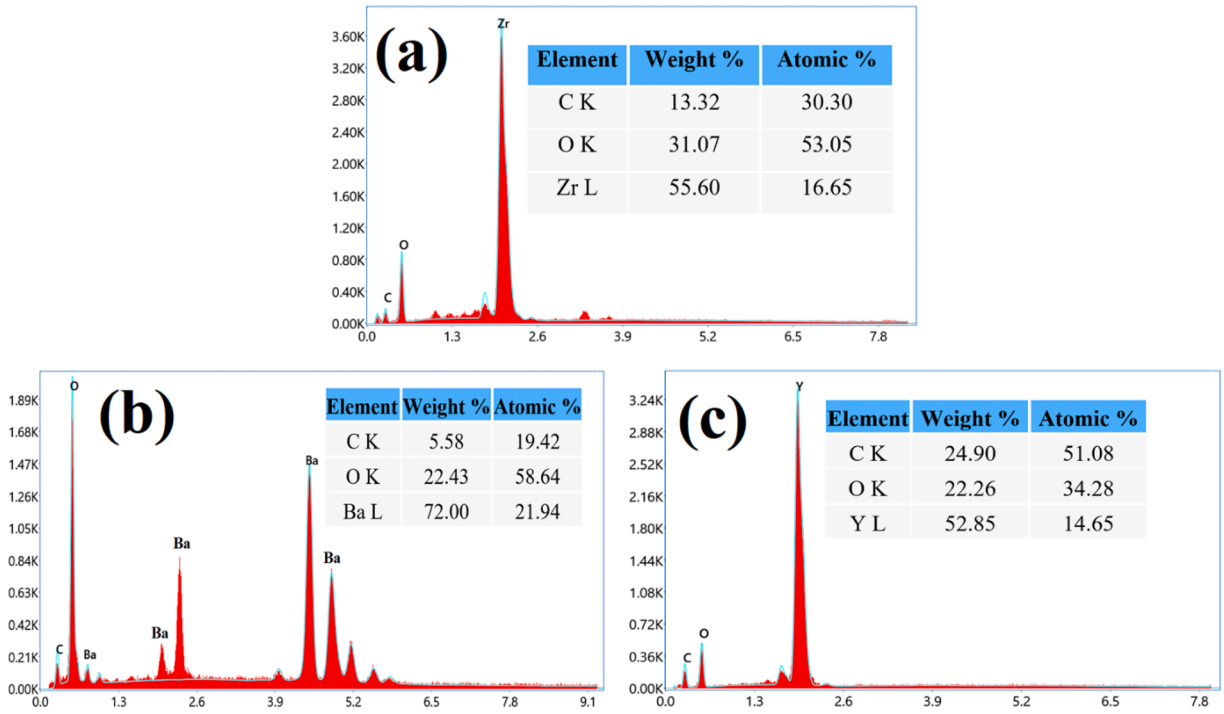


Fig. 5. Elemental composition analysis of prepared a) ZrO_2, b) BaO and c) Y_2O_3.

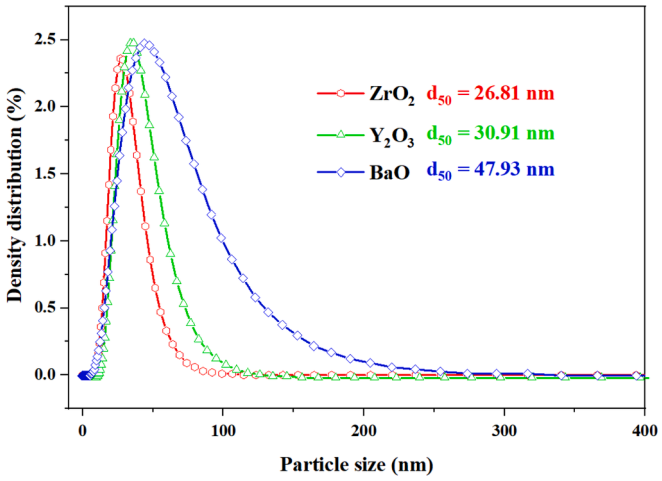


Fig. 6. Particle size analysis of prepared nanoparticles.

This assay allowed the evaluation of the free radical scavenging potential of the nanoparticles based on their ability to reduce the DPPH radicals, which was indicated by a decrease in absorbance at 517 nm. The results were compared across the different samples and concentrations to assess their antioxidant efficiency.

2.8. Photocatalytic activity procedure

The photocatalytic degradation of brilliant blue (BB) and rhodamine B (RhB) dyes using the prepared ZrO_2, BaO, and Y_2O_3 nanoparticles was conducted to assess the efficiency of the catalysts in pollutant removal. Stock solutions of both dyes were prepared by dissolving 15 ppm of BB and RhB in 100 mL of DD water. 10 mg/L of the synthesized nanoparticles were added to the dye solutions to ensure equilibrium adsorption, followed by stirring in the dark for 30 min. This step allowed the dyes to adsorb onto the catalyst surfaces. Subsequently, the solutions were exposed to natural sunlight (~ 800 W/m^2) under constant stirring using a magnetic stirrer at 150 rpm to initiate photocatalytic degradation. The degradation process was allowed to continue until near-complete degradation was achieved. The progress of the degradation was monitored by measuring the absorbance of the solutions every 15 min using a UV–Vis spectrophotometer, with the maximum absorbance wavelengths of 560 nm for BB and 555 nm for RhB. The degradation efficiency of the catalysts was calculated using the formula [33]:

$$\text{Degradation efficiency}\ (\%) = \frac{B_0 - B_t}{B_0} \times 100$$

Where B_0 is the initial concentration of the dye (based on absorbance), and B_t is the concentration at time t.

3. Results and Discussion

3.1. X-ray diffraction analysis

The XRD spectra, as shown in Fig. 2, reveal the characteristic diffraction peaks of the prepared ZrO_2, BaO, and Y_2O_3 nanoparticles, corresponding to their respective crystal structures. For ZrO_2 (Fig. 2 (a)), the predominant peaks observed at specific 2θ positions correspond to the (11–1), (111), and (002) crystal planes, indicative of a Baddeleyite structure. This phase aligns with the standard diffraction data (ICDD: 96–901-6715) and is associated with the monoclinic space group P 1 21/c 1 [34]. Similarly, the BaO nanoparticles (Fig. 2 (b)) exhibit diffraction peaks that match a tetragonal crystal structure, as indexed by the space group P4/m (ICDD: 96–901-3414) [35]. The Y_2O_3 sample (Fig. 2 (c)) displays intense peaks corresponding to the (222), (044), and (226) planes, characteristic of the cubic phase of Yttrium oxide with the space group Ia3 (ICDD:96–720-5918) [36]. The crystalline sizes of the nanoparticles were calculated using the Debye-Scherrer equation [37], revealing average sizes of 19.43 nm, 35.44 nm, and 23.88 nm for ZrO_2, BaO, and Y_2O_3, respectively. The relatively small crystallite sizes indicate effective nucleation and growth of the metal oxide nanoparticles, facilitated by the bioactive compounds in Eucalyptus leaf extract, which

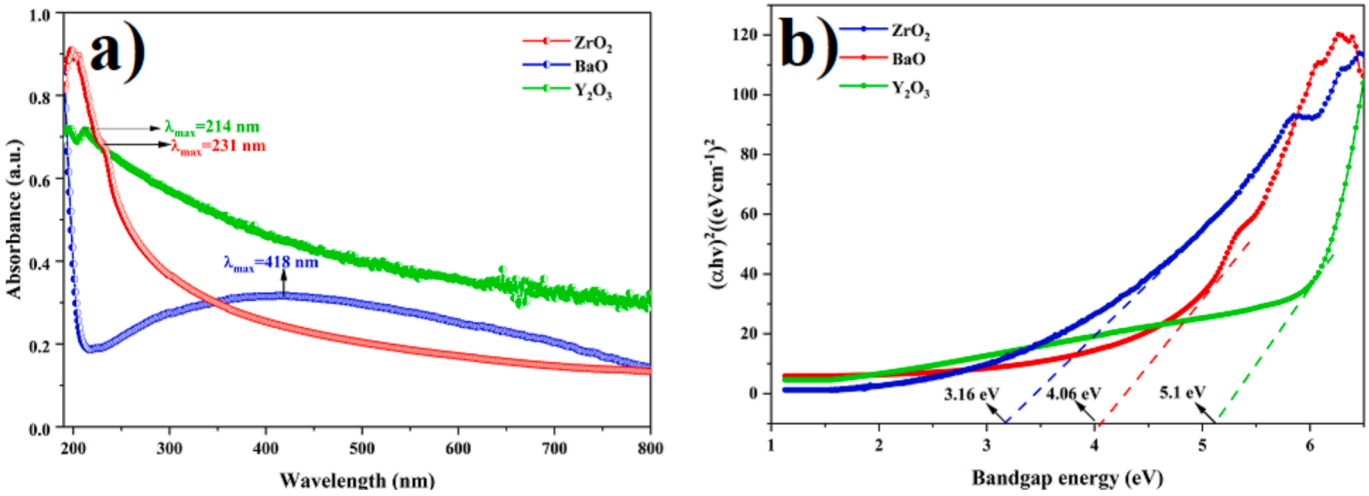


Fig. 7. Optical properties for prepared ZrO_2, BaO, and Y_2O_3 a) Absorbance spectra and b) Optical band gap.

Table 1
Antibacterial zone formation by prepared nanoparticles against *E. coli* and *S. aureus*.

Sample	Zone of inhibition (mm)							
	E. coli				*S. aureus*			
	S25	25 μg/mL	50 μg/mL	100 μg/mL	S25	25 μg/mL	50 μg/mL	100 μg/mL
BaO	12	13	15	18	13	15	19	21
ZrO_2	12	10	13	16	13	13	16	19
Y_2O_3	12	9	12	15	13	10	14	18

acted as both a reducing and capping agent. Further, the dislocation density and microstrain were calculated using equations from previous literature [38,39]. The calculated dislocation density values were 2.65 $\times 10^{-3}$ nm^{-2}, 0.79 $\times 10^{-3}$ nm^{-2}, and 1.75 $\times 10^{-3}$ nm^{-2} for ZrO_2, BaO, and Y_2O_3, respectively. The microstrain values were 0.0125, 0.0083, and 0.0102, respectively. These results suggest that BaO exhibits the lowest dislocation density and microstrain, indicating better crystallinity than ZrO_2 and Y_2O_3. The overall structural analysis highlights the high-quality crystalline nature of the synthesized nanoparticles, with minimal lattice imperfections.

3.2. Functional group analysis

The functional groups present in the prepared samples were analyzed using FTIR spectroscopy to assess phase purity and evaluate the role of *Eucalyptus leaf* extract in stabilizing the nanoparticles. As shown in Fig. 3, several predominant peaks were observed in the spectra. A broad peak at 3442 cm^{-1} across all samples is attributed to O–H stretching vibrations, likely due to adsorbed atmospheric moisture or residual KBr used in pellet preparation [40]. The peak observed at 1625 cm^{-1} corresponds to C=O stretching vibrations, indicating the presence of carboxyl groups derived from the *Eucalyptus* leaf extract, which may play a crucial role in capping and stabilizing the nanoparticles [41]. The bending vibration observed at 1101 cm^{-1} is associated with H–C–H groups, characteristic of methylene functional groups found in the organic composition of the extract [42,43].

Additionally, peaks within the 1000–500 cm^{-1} region are characteristic of metal–oxygen (M−O) bonds, confirming the formation of metal oxides. Specifically, for ZrO_2, a prominent peak at 622 cm^{-1} is attributed to Zr–O stretching vibrations [44]. Similarly, the Ba–O and Y–O bonds in BaO and Y_2O_3 samples are identified at 605 cm^{-1} and 574 cm^{-1}, respectively [45,46]. The absence of extraneous peaks in the FTIR spectra indicates the formation of phase-pure metal oxide structures, effectively functionalized and stabilized by the *Eucalyptus* leaf extract.

3.3. Morphology and elemental analysis

The surface morphology and structural characteristics of the prepared ZrO_2, BaO, and Y_2O_3 nanoparticles were examined using FESEM at different magnifications, as shown in Fig. 4 (a–f). Fig. 4 (a) and (b) depict the FESEM images of ZrO2 nanoparticles at 500 nm and 200 nm magnifications, respectively. The photos reveal a uniform and compact structure with well-defined grain boundaries. The ZrO_2 nanoparticles exhibit a semi-spherical morphology with minimal agglomeration. The observed surface texture suggests the presence of interstitial Zr^{3+} ions, consistent with the monoclinic phase of ZrO_2.

The relatively smooth particle surfaces further indicate effective stabilization, likely influenced by using the *Eucalyptus* leaf extract during synthesis. The BaO nanoparticles, as seen in Fig. 4 (c and d), exhibit a predominantly spherical morphology, with moderate agglomeration evident at higher magnifications. The particles appear relatively monodisperse, indicating uniform size distribution. The surface morphology of BaO also indicates enhanced particle stability and high specific surface area, which can contribute to its photocatalytic efficiency. The Y_2O_3 samples, as seen in Fig. 4 (e and f), display a distinct flaky and layered morphology, with a non-spherical, irregular structure. The particles exhibit significant agglomeration, forming dense clusters. This unique morphology could provide an extended reactive surface area, potentially enhancing the material's interaction with pollutant molecules during photocatalytic applications. The structural features also suggest the role of the synthesis process and the stabilizing agent in influencing particle growth and morphology.

The elemental composition of the synthesized ZrO_2, BaO, and Y_2O_3 nanoparticles was analyzed using EDAX, as shown in Fig. 5 (a–c). The EDAX spectrum of ZrO_2 nanoparticles (Fig. 5(a)) displays prominent peaks corresponding to zirconium (Zr), oxygen (O), and carbon (C). Zirconium accounts for 55.60 % by weight and 16.65 % by atomic percentage, indicating its dominance in the sample composition. The EDAX spectrum of BaO nanoparticles (Fig. 5 (b)) shows characteristic peaks for barium (Ba), oxygen (O), and carbon (C). Barium is the major element, with a weight percentage of 72.00 % and an atomic percentage of 21.94 %, confirming the successful synthesis of BaO. The EDAX spectrum of Y_2O_3 nanoparticles (Fig. 5(c) identifies yttrium (Y), oxygen (O), and carbon (C) as the primary elements. Yttrium accounts for 52.85 % by weight and 14.65 % by atomic percentage, confirming the formation of Y_2O_3. All samples are detected with the minimum rate of

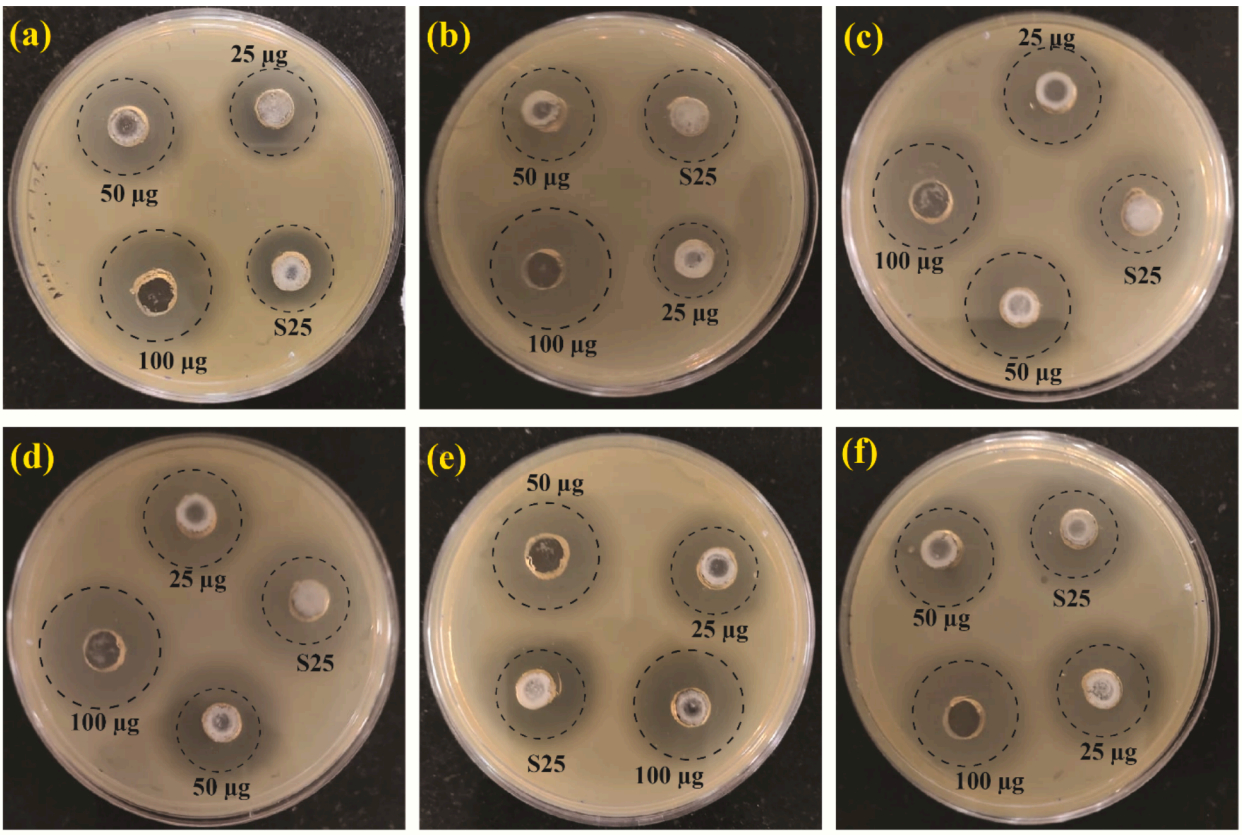


Fig. 8. Antibacterial zone of inhibition for ZrO_2, BaO, and Y_2O_3 for *E. coli* (a-c) and *S. aureus* (d-f).

carbon constituents, which could have arisen due to the capping agent employed or adsorbed atmospheric carbon species. The detection of attachment of carbon groups in the samples is consistent with the FTIR results showing the effective functionalization of *Eucalyptus* leaf as a capping agent.

3.4. Particle size analysis

The particle size distribution of the synthesized ZrO_2, BaO, and Y_2O_3 nanoparticles was analyzed using a particle size analyzer, and the results are presented in Fig. 6. The data reveal a clear distinction in particle size distribution among the samples, with median particle sizes (d_{50}) for ZrO_2, BaO, and Y_2O_3 being 26.81, 47.93, and 30.91 nm. The particle size of prepared samples correlates with the crystalline size observed in the Debye-Scherrer equation. The smaller particle size of ZrO_2 indicates a highly effective nucleation process facilitated by the *Eucalyptus leaf* extract as a capping and reducing agent. The moderate particle size observed for Y_2O_3 reflects its uniform growth and dispersion. BaO nanoparticles exhibit the largest particle size among the samples, suggesting a tendency for agglomeration during synthesis, likely due to differences in the ionic nature and crystal growth mechanism. The relatively narrow distribution range for all samples indicates the successful synthesis of nanoparticles with controlled size and morphology. Smaller particles, such as ZrO_2, are expected to have a higher surface area, which could enhance their photocatalytic and antibacterial activities. These observations correlate well with the XRD analysis, where the calculated crystalline sizes using the Debye-Scherrer equation align with the particle size trends obtained from PSA. The results confirm the capability of the green synthesis approach in controlling particle size and distribution while maintaining the structural and morphological properties required for advanced applications. This demonstrates the effectiveness of *Eucalyptus* leaf extract in producing nanoparticles with tailored characteristics for environmental and biological applications.

3.5. Uv–vis spectroscopy

The UV–visible absorbance spectra of the prepared ZrO_2, BaO, and Y_2O_3 nanoparticles, recorded in the wavelength range of 190–800 nm (Fig. 7(a)), reveal distinct absorption characteristics. The maximum absorbance peaks were observed at 214 nm, 231 nm, and 418 nm for ZrO_2, BaO, and Y_2O_3, respectively. As reported in earlier studies, the absorbance peak for ZrO2 nanoparticles aligns well with its monoclinic crystal structure, which is associated with interstitial Zr^{3+} ions [47]. For BaO nanoparticles, a strong shoulder absorption feature is evident in the visible region, highlighting their excellent optical properties as visible-light-driven photocatalysts. The absorbance spectrum of Y_2O_3 nanoparticles displays a strong peak in the UV region, accompanied by a weak shoulder in the visible region, suggesting limited visible-light activity. To further analyze their optical properties, the band gaps of the samples were determined using Tauc plots. As depicted in Fig. 7 (b), the calculated optical band gaps are 4.06 eV for ZrO_2, 3.16 eV for BaO, and 5.1 eV for Y_2O_3. Generally, an optimal band gap for photocatalytic applications lies in the 1.2–3.5 eV range, enabling efficient light absorption and charge separation under visible light [48,49]. Among the prepared samples, BaO demonstrates a band gap within this optimal range, making it particularly effective for photocatalysis. The narrower band gap of BaO facilitates enhanced absorption of visible light and promotes efficient charge transfer, minimizing the recombination of photogenerated electron-hole pairs [50]. This characteristic improves the generation of reactive oxygen species (ROS), such as hydroxyl radicals (•OH) and superoxide radicals (O_2^{-}), which are crucial for photocatalytic degradation [51]. Consequently, due to their favourable optical properties and sustained charge separation, BaO nanoparticles demonstrate strong potential as effective photocatalysts in visible-light-driven reactions.

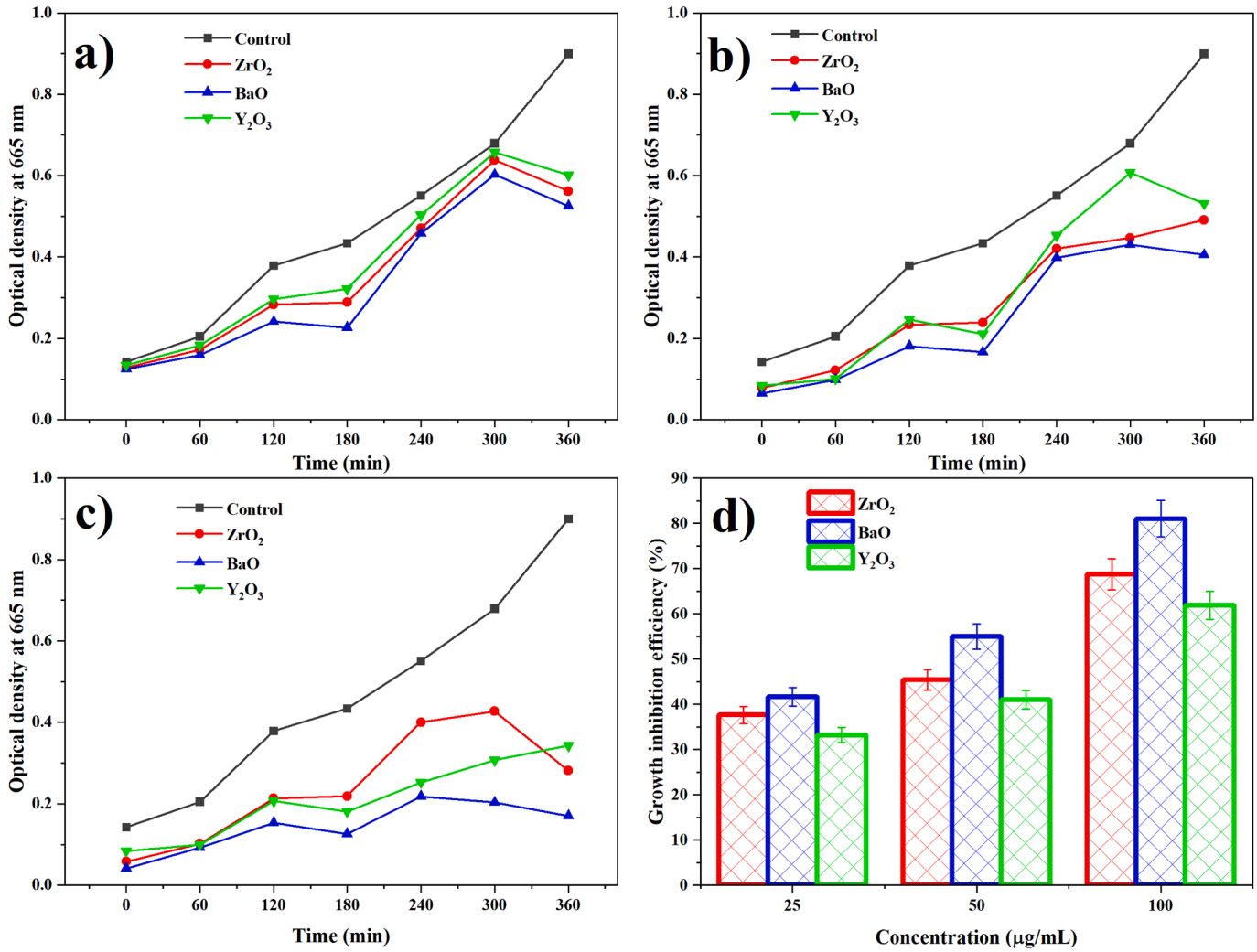


Fig. 9. Bacterial growth reduction activity against *E. coli* with prepared nanomaterials at a) 25 μg/mL, b) 50 μg/mL, and c) 100 μg/mL concentration, and d) growth inhibition efficiency.

3.6. Antibacterial activity

The antibacterial activity of the synthesized BaO, ZrO_2, and Y_2O_3 nanoparticles demonstrated significant zone formation against *E. coli* and *S. aureus* in a concentration-dependent manner. Table 1 highlights the highest zones of inhibition observed at a concentration of 100 μg/mL. Specifically, as seen in Fig. 8, inhibition zones for BaO, ZrO_2, and Y_2O_3 nanoparticles were 18, 16, and 13 mm against *E. coli* and 21, 19, and 18 mm against *S. aureus*, respectively. These results confirm that all synthesized nanoparticles exhibited notable antibacterial efficacy, with BaO showing superior activity. The enhanced antibacterial effect of BaO nanoparticles can be attributed to their smaller particle size, which facilitates penetration through bacterial cell walls and disruption of intracellular components such as proteins and DNA [52].

The antibacterial mechanism of the prepared nanoparticles is likely initiated by targeting the bacterial cell membrane. This involves several disruptive processes, including interference with periplasmic functions, inhibition of dehydrogenase activity, and disruption of key metabolic pathways by adhering to the bacterial surface. Once internalized, the smaller particles exacerbate cellular damage by inducing leakage of intracellular contents, ultimately resulting in bacterial cell death. Interestingly, the nanoparticles exhibited greater antibacterial efficacy against *S. aureus* than *E. coli*. This difference can be ascribed to variations in the structural and surface characteristics of the bacteria. Unlike *E. coli*, which has an outer membrane enriched with lipopolysaccharides that act as a barrier, *S. aureus* lacks this protective layer, making its peptidoglycan membrane more susceptible to nanoparticle penetration.

Additionally, the moderately negative surface charge of *S. aureus* is lower than that of *E. coli*, promoting stronger electrostatic interactions with negatively charged reactive oxygen species (ROS) generated by the nanoparticles [53]. This enhances oxidative stress and cellular damage in *S. aureus* compared to *E. coli*. Overall, the synthesized nanoparticles demonstrated substantial antibacterial activity, highlighting their potential for applications in clinical and healthcare settings.

3.7. Bacterial growth reduction activity

Quantitative analysis of the antibacterial efficacy of the synthesized ZrO_2, BaO, and Y_2O_3 nanoparticles is essential to evaluate their potential applications and validate their practical implications. Many real-world applications, such as infection treatment, coatings, and liquid-based disinfection systems, involve bacterial exposure in aqueous environments. The turbidimetric analysis provides insights into the effectiveness of antibacterial agents under such conditions. As depicted in Fig. 9, the optical density (OD) values for *E. coli* initially increased during incubation with the nanoparticles, indicating bacterial growth. However, after 300 min (5 h), a marked decrease in OD values was observed, confirming bacterial cell death. Notably, at higher nanoparticle concentrations (100 μg/mL), the OD values began to decline as early as 240 min, suggesting faster inhibition of bacterial growth than at lower

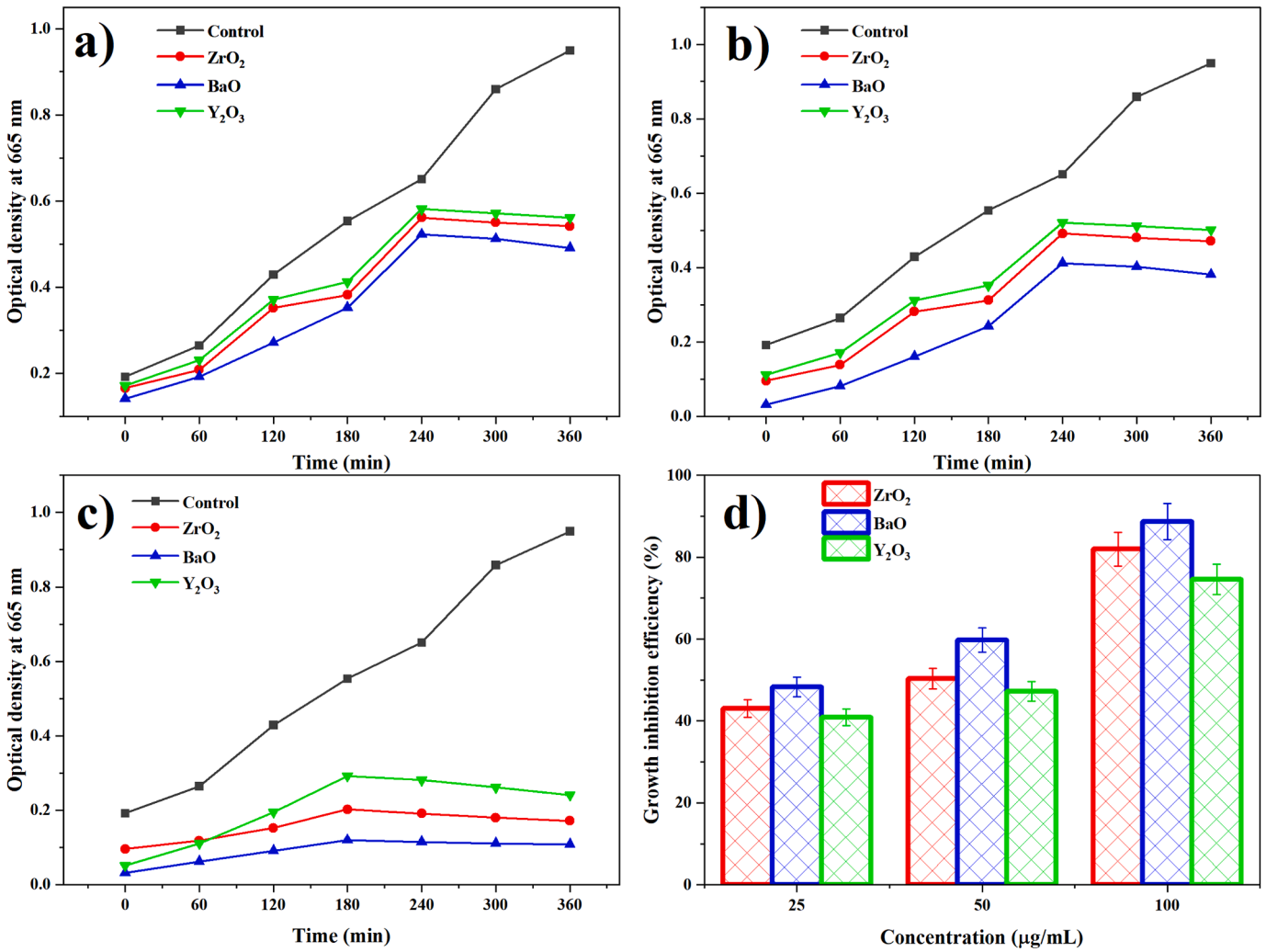


Fig. 10. Bacterial growth reduction activity against *S. aureus* with prepared nanomaterials at a) 25 µg/mL, b) 50 µg/mL, and c) 100 µg/mL concentration and d) growth inhibition efficiency.

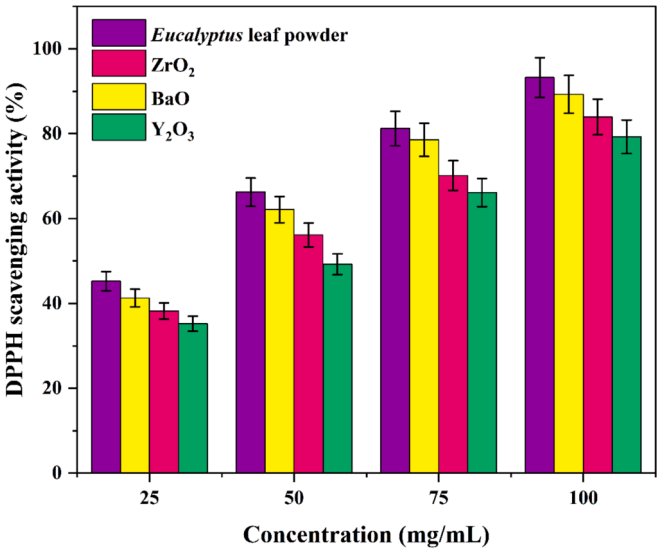


Fig. 11. Antioxidant activity of *Eucalyptus* and prepared BaO, ZrO_2, and Y_2O_3 nanoparticles.

concentrations (25 and 50 µg/mL). The growth inhibition efficiency against *E. coli* increased from 37.6 %, 41.6 %, and 33.1 % for ZrO_2, BaO, and Y_2O_3 nanoparticles at 25 µg/mL to 68.7 %, 81.4 %, and 61.8 %, respectively, at 100 µg/mL.

Similarly, for *S. aureus*, faster growth reduction was observed than for *E. coli.* As shown in Fig. 10, at lower concentrations (25 and 50 µg/mL), OD values began decreasing at 240 min, while at 100 µg/mL, the reduction started earlier, at 180 min (3 h). The growth inhibition efficiency of ZrO_2, BaO, and Y_2O_3 nanoparticles against *S. aureus* increased from 43.2 %, 48.2 %, and 40.8 % at 25 µg/mL to 81.9 %, 88.6 %, and 74.5 % at 100 µg/mL, respectively. The higher susceptibility of *S. aureus* (Gram-positive) compared to *E. coli* (Gram-negative) is likely due to structural differences. *S. aureus* lacks the outer lipopolysaccharide layer of *E. coli*, which acts as a protective barrier, making it more vulnerable to nanoparticle penetration [31]. Furthermore, the lower surface charge of *S. aureus* facilitates stronger interactions with reactive oxygen species (ROS) generated by the nanoparticles, enhancing bacterial damage. Among the tested nanoparticles, BaO demonstrated the highest antibacterial efficacy against *E. coli* and *S. aureus* at all evaluated concentrations. This can be attributed to its smaller particle size, enabling efficient penetration of bacterial cell walls and subsequent intracellular disruption. Overall, the growth inhibition activity of the synthesized nanoparticles highlights their potential for practical applications, particularly in sanitation and disinfection protocols.

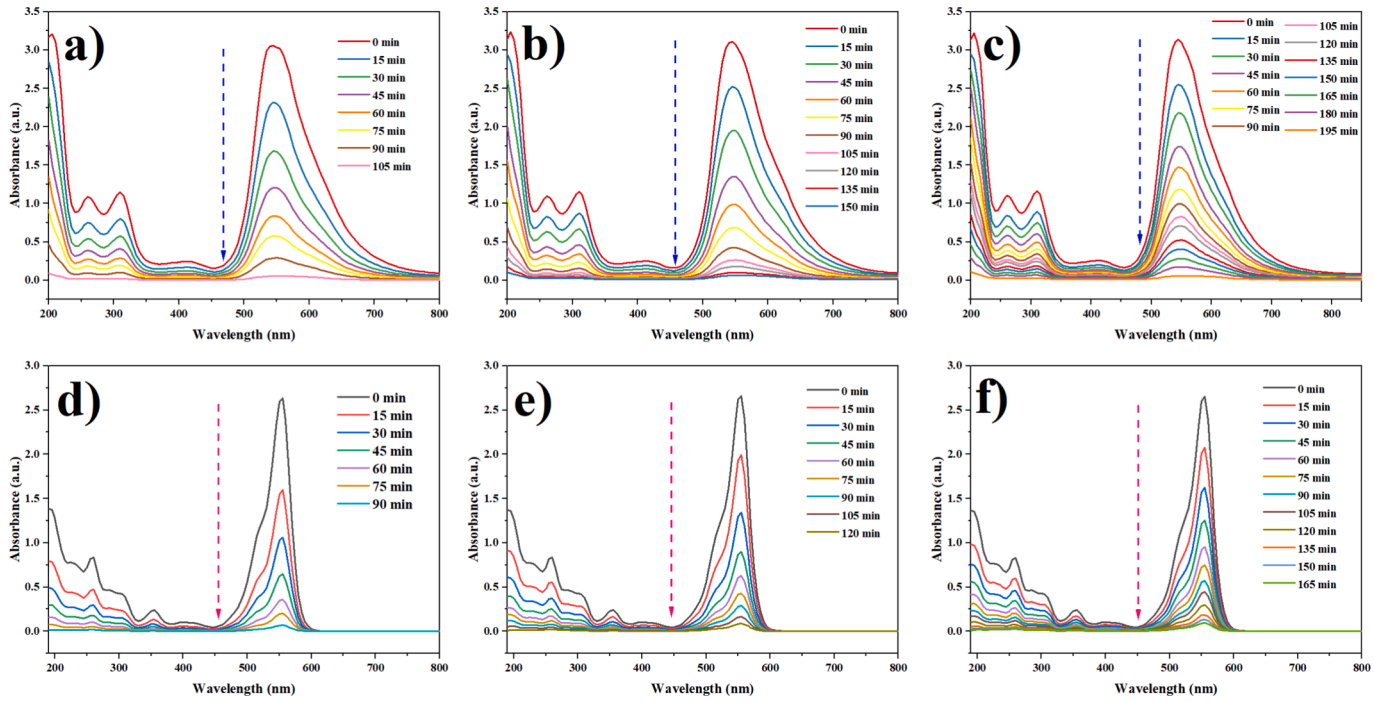


Fig. 12. Absorbance spectra at the maximum intensity of BB dye with prepared nanocatalyst a) ZrO_2, b) BaO, c) Y_2O_3, and for RhB dye d) ZrO_2, e) BaO, and f) Y_2O_3.

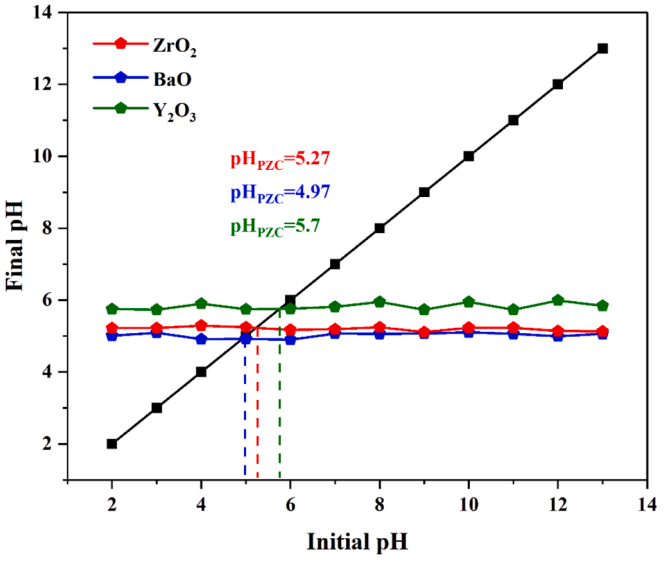


Fig. 13. Point of zero charge of prepared nanocatalyst.

3.8. Antioxidant activity

The antioxidant potential of nanoparticles is a critical factor enabling their application across diverse fields. Antioxidant nanoparticles are vital in mitigating oxidative stress-related disorders, including cardiovascular diseases caused by free radicals in the human body. Additionally, they are extensively used in polymers, fuels, and lubricants to prevent damage induced by free radicals generated through UV radiation and heat exposure. This study evaluated the antioxidant activity of BaO, ZrO2, and Y2O3 nanoparticles synthesized using Eucalyptus leaf powder using the DPPH radical scavenging assay. As illustrated in Fig. 11, the DPPH scavenging activity of the samples increased with the concentration, ranging from 25 to 100 mg/mL. Specifically, the scavenging efficiencies at 25 mg/mL were 45.2 %, 41.2 %, 38.3 %, and 35.1 % for *Eucalyptus*, BaO, ZrO_2, and Y_2O_3, respectively, which raised to 93.2 %, 89.6 %, 83.9 %, and 79.26 % at 100 mg/mL. The superior antioxidant activity of *Eucalyptus* leaf powder (93.2 %) is attributed to its high content of phenolic compounds, which are known for their potent free radical scavenging capabilities. These phytochemicals act through hydrogen or sequential proton loss electron transfer (SPLET) mechanisms, stabilizing reactive oxygen species. OH, and ROO radicals [52]. The BaO nanoparticles also exhibited significant antioxidant activity (89.6 % at 100 mg/mL), underscoring their potential utility in various applications. The antioxidant mechanism of the synthesized nanoparticles is likely multifaceted. The first pathway involves the attachment of phytochemicals from the *Eucalyptus* extract, as evidenced by FTIR analysis, which facilitates free radical scavenging and stabilization. The second mechanism is intrinsic to the nanoparticles, resembling enzyme-mimetic antioxidant activity, a unique property of semiconductor nanoparticles [54]. These findings suggest that the synergistic antioxidant potential of phytochemical-enriched semiconductor nanoparticles can be harnessed for practical applications in water treatment, packaging, and polymer industries.

3.9. Photocatalytic activity

The photocatalytic activity of the synthesized BaO, ZrO_2, and Y_2O_3 catalysts was evaluated using BB and RhB as model pollutants and monitored until maximum degradation efficiencies were achieved. Initially, the dye solution was added with a catalyst, and the adsorption efficiency was evaluated separately, where the overall adsorption efficiency under dark conditions was less than ~ 6 %, suggesting that irradiation is necessary to undergo photocatalytic mineralization of dye molecules. As shown in Fig. 12, the absorbance spectra of RhB and BB recorded at 15-minute intervals exhibit a consistent decrease in peak absorbance, signifying progressive degradation of the pollutants. The maximum degradation efficiencies for BB using ZrO_2, BaO, and Y_2O_3 were 98.64 %, 99.18 %, and 98.78 % at 150, 105, and 195 min, respectively. Similarly, RhB degradation efficiencies achieved were 98.61 %, 98.9 %, and 98.3 % at 120, 90, and 165 min, respectively. Notably, BaO demonstrated the highest degradation rate for both dyes in the shortest duration compared to the other catalysts, which can be

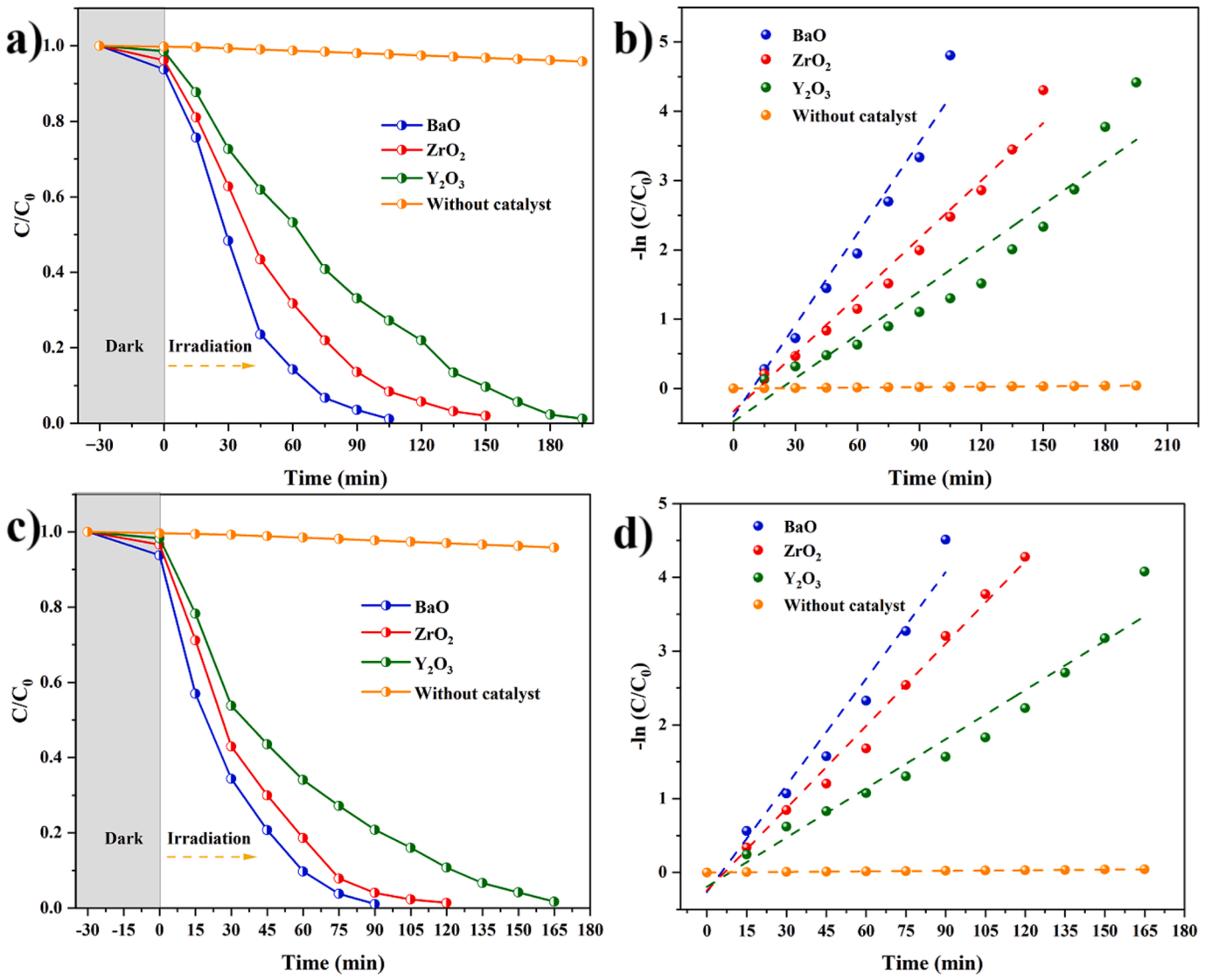


Fig. 14. C/C_0 and kinetic fit for the degradation of BB (a and b) and RhB (c and d).

Table 2
Kinetic values obtained for prepared nanocatalyst.

Nanocatalyst	Maximum efficiency (%)		Time taken (min)		Kinetic rate (min^{-1})		R^2	
	BB	RhB	BB	RhB	BB	RhB	BB	RhB
ZrO_2	98.64	98.61	150	120	2.7×10^{-2}	3.7×10^{-2}	0.974	0.987
BaO	99.18	98.9	105	90	4.3×10^{-2}	4.8×10^{-2}	0.961	0.976
Y_2O_3	98.78	98.3	195	165	2.08×10^{-2}	2.2×10^{-2}	0.963	0.966

attributed to its favourable properties, including a lower band gap energy (3.16 eV), smaller particle size, unique morphology, and enhanced absorption in the visible spectrum. The reduced band gap of BaO facilitates efficient electron excitation from the valence band to the conduction band, enhancing charge carrier transfer to the Fermi level of the dye molecules. Moreover, the smaller particle size of BaO, synthesized under optimized conditions, increases the surface area and provides abundant active sites for dye-catalyst interactions, accelerating the degradation process. In contrast, the ZrO_2 catalyst, with the second-lowest band gap among the tested materials, exhibited higher photocatalytic activity than Y_2O_3 due to its enhanced visible-light absorption and efficient charge separation.

Notably, the maximum degradation of RhB dye by the synthesized nanocatalysts was achieved in a shorter time than BB dye, which can be attributed to the influence of point of zero charge (pH_{PZC}) measurements, as illustrated in Fig. 13. The pH_{PZC} values for the prepared ZrO_2, BaO, and Y_2O_3 nanocatalysts were found to be 5.27, 4.97, and 5.7, respectively, all lower than the pH values of RhB (6.8) and BB (6.2). This enhanced adsorption fosters more efficient electron transfer and rapid degradation of RhB. In contrast, BB dye, which is anionic, carries a negative surface charge, leading to electrostatic repulsion from the similarly charged catalyst surface when the pH exceeds the pH_{PZC}. This repulsive interaction reduces adsorption efficiency, resulting in slower degradation of BB compared to RhB. The findings suggest that the pH_{PZC} of the nanocatalysts plays a pivotal role in adsorption dynamics, enabling more efficient degradation of cationic dyes like RhB. These

Table 3
Comparison table with various transition metal oxide nanoparticles.

Sample	Reducing agent	Sample Conc.	Pollutant	Pollutant Conc.	Source of light	Degradation efficiency (%)	Reaction time	Ref
ZrO_2	*Wrightia tinctoria* leaf	0.05 g	Reactive yellow	10 mg	Sunlight	94	120	[56]
ZrO_2	*Lagerstroemia speciosa*	0.2 g	Methyl orange	10 mg	Sunlight	94.58	290	[57]
Y_3O_4	*Lantana camara L.*	20 mg	Rhodamine B	10 ppm	UV–Vis	92	60	[58]
ZrO_2	*Sonchus asper aqueous*	10 mg	Methyl blue	10 ppm	UV	93	180	[59]
ZrO_2	*Murraya koenigii*	10 mg	Methylene blue	10 ppm	Visible	94	20	[60]
Y_3O_4	*Aloe vera gel*	60 mg	Metanil yellow	10 ppm	UV	79	90	[61]
$ZnFe_2O_4$/ Y_2O_3	*Citrus limon (L.)*	8 mg	Malachite green	9×10^{-5}	Visible	95.44	120	[62]
Y_2O_3:Eu^{3+}	*Aloe Vera gel*	60 mg	Methyl blue	10 ppm	UV	81	120	[63]
BaO	NaOH	20 mg	Malachite green	50 ppm	UV	86.6	120	[50]
BaO	KOH	25 mg	Rhodamine B	2×10^{-5} M	Visible	99	60	[64]
BaO	NaOH	150 mg	Rhodamine B	1×10^{-5} M	UV	85	160	[65]
BaO	*Eucalyptus*	10 mgL^{-1}	Rhodamine B	15 ppm	Sunlight	98.9	90	Present work
			Brilliant blue			99.18	105	

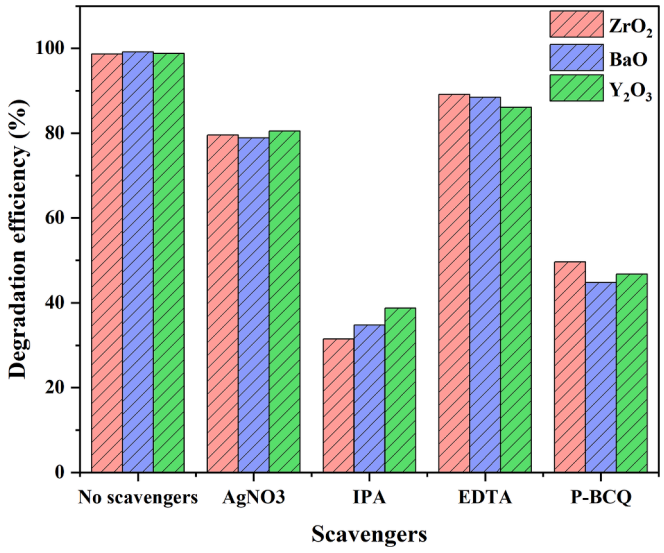


Fig. 15. Quenching activity performed with different scavengers for determining the degradation pathway of prepared catalyst on a) RhB and b) BB dyes.

insights underscore the significance of pH and catalyst surface charge interactions in optimizing photocatalytic efficiency for diverse dye pollutants.

3.10. Kinetics study

As the degradation efficiencies of RhB and BB dyes reach maximum levels with the synthesized nanocatalysts, assessing the rate constants is essential to enable a comparative analysis of the ZrO_2, BaO, and Y_2O_3 nanocatalysts. To quantify the kinetics, a pseudo-first-order degradation model was applied, and the data were fitted using the Langmuir-Hinshelwood model based on the following equation [55]:

$$\ln\frac{C}{C_0} = kt$$

C and C_0 are the concentration of the pollutant at time (t) and the initial concentration of the pollutant. The kinetic apparent rate constant is represented as k. Fig. 14 (a and c) shows the reduction in dye concentration over time for BB and RhB dyes in the presence of each catalyst, while the kinetic fit curves are illustrated in Fig. 14 (b and d). The rate constant k for the degradation of both dyes showed an upward trend with increased exposure time, highlighting the influence of the catalyst's surface interactions over prolonged photocatalytic exposure. As detailed in Table 2, BaO nanoparticles exhibit a significantly higher degradation rate than the other catalysts, achieving apparent rate constants of 4.3 $\times$ 10^{-2} and 4.8 $\times$ 10^{-2} min^{-1} for BB and RhB, respectively, with strong correlation coefficients (R^2). This enhanced degradation rate can be attributed to BaO's optimized band gap and favourable surface properties, which promote efficient pollutant breakdown. Under sunlight irradiation, these features, particularly the narrowed band gap and extended absorption within the visible spectrum, facilitate the generation and transfer of photogenerated electron-hole pairs, resulting in the effective degradation of dye molecules. Comparative analysis of the degradation efficiency of the synthesized nanocatalysts with other semiconductor metal oxides (see Table 3) further underscores the superior performance of the prepared catalysts at reduced concentrations, indicating that BaO nanoparticles are particularly well-suited for environmental remediation applications due to their unique electronic and surface characteristics.

3.11. Scavenging activity

A scavenging test was performed to elucidate the degradation mechanism of RhB and BB with a prepared nanocatalyst. This study involved the scavenging of photogenerated electrons (e^-), holes (h^+), hydroxyl radical (·OH), and superoxide species ($O_2^{\cdot-}$) with 100 mM concentrations of $AgNO_3$, EDTA, P-BCQ, and IPA, respectively. The reaction was carried out with a similar duration for the degradation activity. Fig. 15 (a) shows that the degradation efficiency of ZrO_2, BaO, and Y_2O_3 against BB significantly reduced to 30.1, 34.7, and 38.7 with the addition of IPA. This signifies that the scavenging of hydroxyl groups produced from semiconductor nanocatalysts by IPA significantly reduced the degradation activity of the catalyst [66]. Using P-BCQ scavengers also considerably reduced the degradation efficiency of prepared nanocatalysts by an average of 50 %, signifying the potential involvement of superoxide ion species in the degradation of BB dye [67]. A similar trend was observed for RhB dye with IPA and P-BCQ scavengers. Though the degradation efficiency was minimally reduced with the usage of AgNO3 and EDTA, a significant decrease in degradation efficiency was observed for IPA and P-BCQ. These results demonstrate that the degradation of BB and RhB dyes was predominantly dependent on the. OH and superoxide ions.

3.12. Degradation mechanism

As illustrated in Fig. 16, the proposed degradation mechanism of the BaO, ZrO_2, and Y_2O_3 nanocatalyst against RhB and BB dyes is initiated through the absorption of photons from sunlight. Upon irradiation, the catalyst absorbs photons with sufficient energy to excite electrons (e^-) from the valence band (VB) to the conduction band (CB), thereby creating electron-hole pairs (e^-/h^+) [68]. These photogenerated charge carriers are critical in driving the subsequent generation of reactive oxygen species (ROS). The excited electrons react with dissolved oxygen molecules in the reaction system, producing superoxide radicals ($O_2^{\cdot-}$)

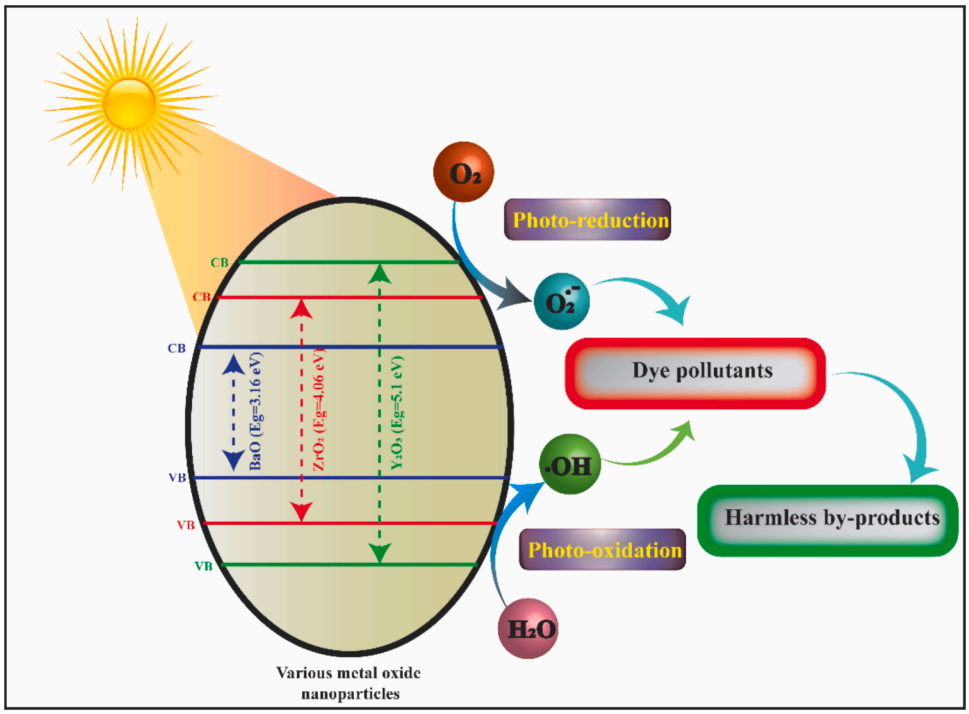


Fig. 16. Degradation mechanism of prepared ZrO_2, BaO, and Y_2O_3 samples.

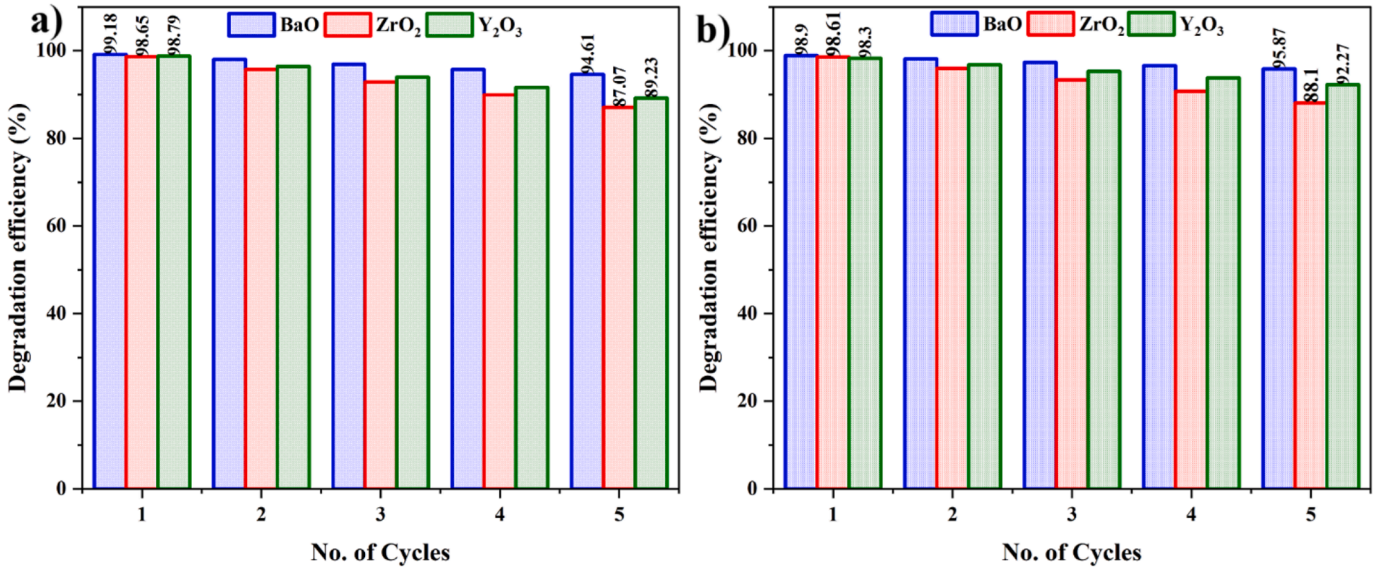


Fig. 17. Cyclic stability of prepared nanocatalyst ZrO_2, BaO, and Y_2O_3 for BB dyes (a) and RhB dyes (d).

[69]. Simultaneously, the photogenerated holes facilitate the oxidation of water molecules or hydroxide ions (OH^-) to generate hydroxyl radicals (•OH). These highly reactive ROS, confirmed by quenching experiments, play a pivotal role in degrading the RhB and BB dye molecules. The ROS interacts with the aromatic structures of the dyes, leading to the oxidative cleavage of benzene rings and the formation of intermediate organic compounds [70]. These intermediates undergo further oxidation via continuous interaction with ROS, breaking down into simpler byproducts such as H_2O and CO_2.

Additionally, the degradation efficiency is significantly influenced by secondary factors, such as the surface charge of the catalyst particles [71,72]. The negatively charged catalyst surface enhances electrostatic interactions with the positively charged dye molecules, promoting greater dye adsorption onto the catalyst surface. This increased proximity between the dyes and the catalyst's active sites enhances the photocatalytic degradation process, making it more effective.

$$Metaloxide[ZrO2/BaO/Y2O3] + hv \rightarrow e^-_{CB} + h^+_{VB}$$

$$e^-_{CB} + O_2 \rightarrow \bullet O^-_2$$

$$h^+_{VB} + H_2O \rightarrow \bullet OH + H^+$$

$$h^+_{VB} + OH^- \rightarrow \bullet OH$$

$$Pollutant(Rhb/BB) + \bullet OH/\bullet O^-_2 \rightarrow Degradationintermediates \rightarrow CO_2 + H_2O$$

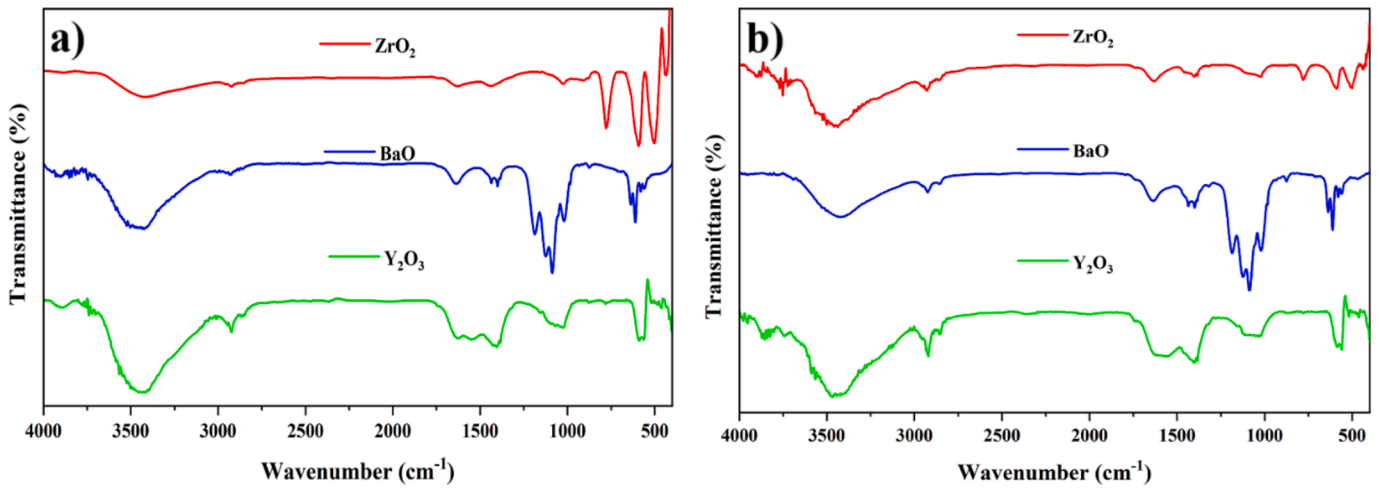


Fig. 18. FTIR spectra of the prepared nanocatalyst after five cycles of degradation against a) BB and b) RhB pollutant.

3.13. Cyclic stability

The reusability of the synthesized nanocatalysts was assessed by evaluating their degradation efficiency over five consecutive cycles under identical reaction conditions. After each cycle, the catalysts were recovered via centrifugation, followed by washing with ethanol and deionized water to remove residual dye and impurities. As depicted in Fig. 17, the degradation efficiency loss for Brilliant Blue (BB) dye after five cycles was 14.58 %, 4.57 %, and 9.55 % for ZrO_2, BaO, and Y_2O_3 nanoparticles, respectively. Similarly, for Rhodamine B (RhB), the degradation efficiency loss was 10.51 %, 3.03 %, and 6.03 % for the same nanocatalysts. Among the tested nanocatalysts, BaO nanoparticles exhibited the lowest degradation efficiency loss for both BB and RhB dyes, demonstrating excellent cyclic stability and reusability. This performance can be attributed to the higher surface area and smaller particle size of BaO nanoparticles, which enhance their catalytic activity and structural stability. However, a minor loss in degradation efficiency observed with BaO could also result from sample loss during the centrifugation process. Notably, Y_2O_3 nanoparticles showed greater cyclic stability compared to ZrO_2. This difference may be due to the stronger binding of dye molecules to ZrO_2, which blocks active sites and reduces catalytic efficiency over repeated cycles. In contrast, the weaker interaction between dye molecules and Y_2O_3 helps preserve its active sites, maintaining structural integrity and catalytic performance across cycles.

The structural stability of the prepared nanocatalyst after the 5th cycle was evaluated using FTIR spectroscopy. As seen in Fig. 18, the FTIR spectrum of prepared samples shows the emergence of new peaks between 1500 and 1000 cm-1, possibly due to the sulfonated compounds of the model pollutant. However, no shifts were observed in the Metal oxygen peak vibration, confirming the structural stability of the prepared nanocatalysts. These results highlight the prepared catalyst's robust reusability and cyclic stability, which suggests their potential uses in practical conditions [73].

4. Conclusion

This study successfully demonstrated the synthesis of ZrO_2, BaO, and Y_2O_3 nanoparticles using *Eucalyptus* leaf extract, employing a sustainable green synthesis approach. The prepared nanoparticles exhibited high crystallinity; as confirmed by XRD analysis, BaO showed the lowest dislocation density and microstrain values, highlighting the superior structural quality. Optical characterization revealed significant variation in the band gaps of the sample; BaO's band gap falls within the optimal range for photocatalytic activity, facilitating efficient light absorption and charge separation. This efficiency was evident in photocatalytic tests, where BaO achieved remarkable dye degradation rates of 99 % for both RhB and BB dyes under natural sunlight. Cyclic stability assessments of BaO nanoparticles demonstrated consistent photocatalytic performance over multiple cycles, indicating excellent reusability and stability. Also, BaO exhibited the highest antibacterial and antioxidant activities, outperforming ZrO_2 and Y_2O_3 in inhibition zone measurements and DPPH radical scavenging assays. Integrating high crystallinity, optimal band gap, superior cyclic stability, and robust multifunctional performance positions BaO nanoparticles as a promising candidate for environmental remediation and biological applications. This study highlights the potential of green-synthesized transition metal oxide nanoparticles in addressing environmental and healthcare challenges.

CRediT authorship contribution statement

M. Pushpa: Writing – original draft, Funding acquisition, Formal analysis, Data curation, Conceptualization. **S. Mageswari:** Writing – original draft, Supervision, Formal analysis, Data curation, Conceptualization. **A. Panneerselvam:** Writing – review & editing, Software, Resources, Data curation.

Declaration of competing interest

The authors declare that they have no known competing financial interests or personal relationships that could have appeared to influence the work reported in this paper.

Data availability

Data will be made available on request.

References

[1] R. Kant, Textile dyeing industry an environmental hazard, *Nat. Sci. (irvine)* 04 (2012) 22–26.
[2] C. Desai, K.R. Jain, R. Boopathy, E.D. van Hullebusch, D. Madamwar, Editorial: Eco-sustainable bioremediation of textile dye wastewaters: Innovative microbial treatment technologies and mechanistic insights of textile dye biodegradation, *Front. Microbiol.* 12 (2021) 707083.
[3] K.-T. Chung, Azo dyes and human health: A review *J. Environ, Sci. Health C Environ. Carcinog. Ecotoxicol. Rev.* 34 (2016) 233–261.
[4] S.H. Hashemi, M. Kaykhaii, 2022 Azo dyes: Sources, occurrence, toxicity, sampling, analysis, and their removal methods Emerging Freshwater Pollutants (Elsevier) pp 267–87.
[5] M. Kaykhaii, M. Sasani, S. Marghzari, Removal of dyes from the environment by adsorption process, *Chem Mater. Eng.* 6 (2018) 31–35.

[6] G.A.R. de Oliveira, J. de Lapuente, E. Teixidó, C. Porredón, M. Borràs, D.P. de Oliveira, Textile dyes induce toxicity on zebrafish early life stages, *Environ Toxicol. Chem.* 35 (2016) 429–434.

[7] U. Shanker, M. Rani, V. Jassal, Degradation of hazardous organic dyes in water by nanomaterials, *Environ Chem. Lett.* 15 (2017) 623–642.

[8] M.T. Yagub, T.K. Sen, S. Afroze, H.M. Ang, Dye and its removal from aqueous solution by adsorption: a review, *Adv. Colloid Interface Sci.* 209 (2014) 172–184.

[9] J. Dotto, M.R. Fagundes-Klen, M.T. Veit, S.M. Palácio, R. Bergamasco, Performance of different coagulants in the coagulation/flocculation process of textile wastewater, *J. Clean. Prod.* 208 (2019) 656–665.

[10] J.E. Park, J.-H. Shin, W. Oh, S.-J. Choi, J. Kim, C. Kim, J. Jeon, Removal of Hexavalent chromium(VI) from Wastewater Using Chitosan-Coated Iron Oxide Nanocomposite Membranes, *Toxics* 10 98 (2022).

[11] Q. Yang, J. Hao, Synthesis of metal sulfides via ionic liquid-mediated assembly strategy and their photocatalytic degradation of dyes in water *Colloids Surf, A Physicochem. Eng. Asp.* 633 (2022) 127848.

[12] R. Tanveer, A. Yasar, A.-U.-B. Tabinda, A. Ikhlaq, H. Nissar, A.-S. Nizami, Comparison of ozonation, Fenton, and photo-Fenton processes for the treatment of textile dye-bath effluents integrated with electrocoagulation, *J. Water Proc. engineering* 46 102547 (2022).

[13] S. Karthikeyan, K. Dhanakodi, S. Surendhiran, K. Vanasundari, L. Arunraja, A. T. Rajamanickam, Unveiling the photocatalytic property of La2O3–CuO nanocomposites for organic pollutants in wastewater treatment, *J. Indian Chem. Soc.* 100 (2023) 101104.

[14] K.C. Suresh, S. Surendhiran, P. Manoj Kumar, E. Ranjth Kumar, Y.A.S. Khadar, A. Balamurugan, Green synthesis of SnO2 nanoparticles using Delonix elata leaf extract: Evaluation of its structural, optical, morphological and photocatalytic properties *SN, Appl. Sci.* 2 (2020).

[15] Munawar T, Mukhtar F, Nadeem M S, Riaz M, Naveed ur Rahman M, Mahmood K, Hasan M, Arshad M I, Hussain F, Hussain A and Iqbal F 2020 Novel photocatalyst and antibacterial agent; direct dual Z-scheme ZnO–CeO2-Yb2O3 heterostructured nanocomposite *Solid State Sci.* **109** 106446.

[16] K. Subramani, J.K.S. Ganeshan, S. Srinivasan, N.V.T. Mohanasundaram, A. Incharoensakdi, Hydrothermally and green synthesized TiO2 nanoparticles with high photocatalytic textile industry dye degradation, antibacterial and antioxidant activities, *J. Alloys Compd.* 1017 (2025) 179068.

[17] V. Devabharathi, K.S.G. Jagan, S.R. Priyan, T.M.N. Vidaarth, S. Surendhiran, Y.A. S. Khadar, K. Kandasamy, Rational design of NiO nanoflakes and porous GCN nanocomposite for synergic effectiveness on photocatalytic degradation of industry effluents and biological activity, *Chem. Phys. Impact* 8 (2024) 100637.

[18] I. Rabani, R. Zafar, K. Subalakshmi, H.-S. Kim, C. Bathula, Y.-S. Seo, A facile mechanochemical preparation of Co3O4@g-C3N4 for application in supercapacitors and degradation of pollutants in water, *J. Hazard. Mater.* 407 (2021) 124360.

[19] S. Sardar, T. Munawar, F. Mukhtar, M.S. Nadeem, S.A. Khan, M. Koc, S. Manzoor, M.N. Ashiq, F. Iqbal, Fullerene trigged energy storage and photocatalytic ability of La2O3-ZnO@C60 core-shell nanocomposite *Mater, Sci. Eng. B Solid State Mater. Adv. Technol.* 288 116151 (2023).

[20] N.C. Horti, M.D. Kamatagi, S.K. Nataraj, M.N. Wari, S.R. Inamdar, Structural and Optical Properties of Zirconium Oxide (ZrO2) Nanoparticles: Effect of Calcination Temperature *Nano Ex.* 1 010022 (2020).

[21] O. Długosz, K. Szostak, M. Banach, Photocatalytic properties of zirconium oxide–zinc oxide nanoparticles synthesised using microwave irradiation *Appl, Nanosci.* 10 (2020) 941–954.

[22] R. Renukadevi, R. Sundaram, K. Kasinathan, Barium oxide nanoparticles with robust catalytic, photocatalytic and humidity sensing properties, *Journal of Nanostructures* 10 (2020) 167–176.

[23] V. Kavitha, P. Mahalingam, M. Jeyanthinath, N. Sethupathi, Optical and structural properties of tungsten-doped barium strontium titanate *Mater, Today* 23 (2020) 12–15.

[24] V. Kavitha, J. Mayandi, P. Mahalingam, N. Sethupathi, Structural, optical and electrical studies on zinc doped barium strontium titanate as photo-anode for DSSC device *Mater, Today* 35 (2021) 48–52.

[25] R.-Z. Cao, L.-J. Zhang, L.-Y. Ding, X.-P. Liu, S.-T. Liu, H.-C. Tao, Yttrium -barium oxide as a robust photocatalyst for photocatalytic degradation of organic dyes under visible light *Ceram, Int.* 48 (2022) 31233–31244.

[26] Y. Zhou, Q. Li, J. Zhang, M. Xiang, Y. Zhou, Z. Chen, Y. Chen, T. Yao, Broad spectrum driven Y doped BiO2−x for enhanced degradation of tetracycline: Synergy between singlet oxygen and free radicals, *Appl. Surf. Sci.* 607 (2023) 154957.

[27] F. Mukhtar, T. Munawar, M.S. Nadeem, M.N. ur Rehman, S. Batool, M. Hasan, M. Riaz, K. ur Rehman, F. Iqbal, Highly efficient tri-phase TiO2–Y2O3–V2O5 nanocomposite: structural, optical, photocatalyst, and antibacterial studies, *J. Nanostructure Chem.* 12 (2022) 547–564.

[28] Surbhi, Kumar A, Singh S, Kumari P and Rasane P 2023 Eucalyptus: phytochemical composition, extraction methods and food and medicinal applications *Advances in Traditional Medicine* **23** 369–80.

[29] R. Abiri, N. Atabaki, R. Sanusi, S. Malik, R. Abiri, P. Safa, N.A.A. Shukor, H. Abdul-Hamid, New insights into the biological properties of eucalyptus-derived essential oil: A promising green anti-cancer drug, *Food Rev Int.* 38 (2022) 598–633.

[30] B. Salehi, J. Sharifi-Rad, C. Quispe, H. Llaique, M. Villalobos, A. Smeriglio, D. Trombetta, S.M. Ezzat, M.A. Salem, A. Zayed, C.M. Salgado Castillo, S.E. Yazdi, S. Sen, K. Acharya, F. Sharopov, N. Martins, Insights into Eucalyptus genus chemical constituents, biological activities and health-promoting effects *Trends Food Sci, Technol.* 91 (2019) 609–624.

[31] G. Nandhini, R. Suriyaprabha, W. Maria Sheela Pauline, V. Rajendran, W.K. Aicher, O.K. Awitor, Influence of solvents on the changes in structure, purity, and in vitro characteristics of green-synthesized ZnO nanoparticles from Costus igneus, *Appl. Nanosci.* 8 (2018) 1353–1360.

[32] M. Yamauchi, Y. Kitamura, H. Nagano, J. Kawatsu, H. Gotoh, DPPH Measurements and Structure-Activity Relationship Studies on the Antioxidant Capacity of Phenols, *Antioxidants (basel)* 13 (2024) 309.

[33] S. Karthikeyan, K. Dhanakodi, S. Surendhiran, K.S.G. Jagan, P. Thirunavukkarasu, L. Arunraja, Effect of synthesis parameters on the structural, morphological characteristics, and photocatalytic activity of La2O3 nanoparticles, *J. Indian Chem. Soc.* 100 (2023) 100860.

[34] B. Storr, D. Kodali, K. Chakrabarty, P.A. Baker, V. Rangari, S.A. Catledge, Single-step synthesis process for high-entropy transition metal boride powders using microwave plasma, *Ceramics* 4 (2021) 257–264.

[35] Savunthari K V, Balaji D, Sudheer N, Bathwar M, Rangasamy M, Dhandabani G K, Puente Santiago A R, Shanmugam S, Kong K-V and Vijayaraghavan 2023 Effective photocatalytic degradation of rhodamine-B over Zn-doped BaO_2 and SrO_2 composites under UV and sunlight irradiation *RSC Sustain.* **1** 1511–21.

[36] Zhou X, Wang Y, Liu X, Liang Z and Jin H 2018 Electrodeposition kinetics of Ni/nano-Y2O3 composite coatings *Metals (Basel)* **8** 669.

[37] S. Mustapha, M.M. Ndamitso, A.S. Abdulkareem, J.O. Tijani, D.T. Shuaib, A. K. Mohammed, A. Sumaila, Comparative study of crystallite size using Williamson-Hall and Debye-Scherrer plots for ZnO nanoparticles, *Adv. Nat. Sci. Nanosci. Nanotechnol.* 10 (2019) 045013.

[38] N. Brown, L.K.F. Jr, Microstrain in polycrystalline metals, *Acta Metall.* 9 (1961) 106–111.

[39] K. Venkateswarlu, M. Sandhyarani, T.A. Nellaippan, N. Rameshbabu, Estimation of crystallite size, lattice strain and dislocation density of nanocrystalline carbonate substituted hydroxyapatite by X-ray peak variance analysis *Procedia Mater, Sci.* 5 (2014) 212–221.

[40] K. Kandasamy, S. Surendhiran, K.S.G. Jagan, G.S. Kumar, Y.A.S. Khadar, P. Rajasingh, Green synthesis of CdS Quantum dots for photocatalytic and anti-corrosive applications in aqueous media, *Appl. Surf. Sci. Adv.* 13 (2023) 100364.

[41] V. Kamath, P. Chandra, G.P. Jeppu, Comparative study of using five different leaf extracts in the green synthesis of iron oxide nanoparticles for removal of arsenic from water, *int. J. Phytoremediation* 22 (2020) 1278–1294.

[42] P.S. Desai, F. Desai, A. Patel, B. Parmar, Anticorrosive properties of Eucalyptus (Nilgiris) leaves extract on 2S grade aluminium in acid solutions, *Appl. Surf. Sci. Adv.* 16 100414 (2023).

[43] D. Bejjanki, P. Banothu, V.B. Kumar, P.S. Kumar, Biomass-Derived N-Doped Activated Carbon from Eucalyptus Leaves as an Efficient Supercapacitor Electrode Material *C* 9 (2023) 24.

[44] R.S. Das, S.K. Warkhade, A. Kumar, A.V. Wankhade, Graphene oxide-based zirconium oxide nanocomposite for enhanced visible light-driven photocatalytic activity, *Res. Chem. Intermed.* 45 (2019) 1689–1705.

[45] M.A. Ansari, N. Jahan, Structural and Optical Properties of BaO Nanoparticles Synthesized by Facile Co-Precipitation Method, *Mater. Highlights* 2 (2021) 23.

[46] L. Zhang, Z. Li, F. Zhen, L. Wang, Q. Zhang, R. Sun, F.A. Selim, C. Wong, H. Chen, High sinterability nano-Y2O3 powders prepared via decomposition of hydroxyl-carbonate precursors for transparent ceramics, *J. Mater. Sci.* 52 (2017) 8556–8567.

[47] L. Kumari, W.Z. Li, J.M. Xu, R.M. Leblanc, D.Z. Wang, Y. Li, H. Guo, J. Zhang, Controlled hydrothermal synthesis of zirconium oxide nanostructures and their optical properties *Cryst, Growth Des.* 9 (2009) 3874–3880.

[48] Marchelek M, Diak M, Kozak M, Zaleska-Medynska A and Grabowska E 2016 Some unitary, binary, and ternary non-TiO2 photocatalysts *Semiconductor Photocatalysis - Materials, Mechanisms and Applications* (InTech).

[49] K. Kočí, L. Obalová, Z. Lacný, Photocatalytic reduction of CO2 over TiO2 based catalysts, *Chem. Pap.* 62 (2008) 1–9.

[50] F. Naz, K. Saeed, Synthesis of barium oxide nanoparticles and its novel application as a catalyst for the photodegradation of malachite green dye, *Appl. Water Sci.* 12 (2022).

[51] H. Selim, E.R. Sheha, R. Elshypany, P. Raynaud, H.H. El-Maghrabi, A.A. Nada, Superior photocatalytic activity of BaO@Ag3PO4 nanocomposite for dual function degradation of methylene blue and hydrogen production under visible light irradiation, *Catalysts* 13 363 (2023).

[52] T. Munawar, M. Shahid Nadeem, F. Mukhtar, S. Manzoor, M. Naeem Ashiq, S. Batool, M. Hasan, F. Iqbal, Multifunctional dual Z-scheme heterostructured Sm2O3-WO3-La2O3 nanocomposite: Enhanced electrochemical, photocatalytic, and antibacterial properties, *Adv. Powder Technol.* 34 (2023) 104061.

[53] T. Munawar, S. Yasmeen, F. Mukhtar, M.S. Nadeem, K. Mahmood, M. Saqib Saif, M. Hasan, A. Ali, F. Hussain, F. Iqbal, Zn0.9Ce0.05M0.05O (M = Er, Y, V) nanocrystals: Structural and energy bandgap engineering of ZnO for enhancing photocatalytic and antibacterial activity *Ceram, Int.* 46 (2020) 14369–14383.

[54] Abdullah, Rahman A U, Faisal S, Almostafa M M, Younis N S and Yahya G 2023 Multifunctional Spirogyra-hyalina-mediated barium oxide nanoparticles (BaONPs): Synthesis and applications *Molecules* **28**.

[55] Samrot A V, Ram Singh S P, Deenadhayalan R, Rajesh V V, Padmanaban S and Radhakrishnan K 2022 Nanoparticles, a double-edged sword with oxidant as well as antioxidant properties—A review, *Oxygen* **2** 591–604.

[56] S. Karthikeyan, K. Dhanakodi, S. Surendhiran, K.S.G. Jagan, N. Lenin, L. Dhatchinamurthy, A.T. Rajamanickam, Sonochemical synthesis of Sn-doped La2O3 nanoparticles and its application for the photocatalytic degradation of hazardous pollutants, *J. Mater. Sci.: Mater. Electron.* 34 (2023).

[57] N. Al-Zaqri, A. Muthuvel, M. Jothibas, A. Alsalme, F.A. Alharthi, V. Mohana, Biosynthesis of zirconium oxide nanoparticles using Wrightia tinctoria leaf extract:

Characterization, photocatalytic degradation and antibacterial activities *Inorg, Chem. Commun.* 127 (2021) 108507.
[58] V. Sai Saraswathi, K. Santhakumar, Photocatalytic activity against azo dye and cytotoxicity on MCF-7 cell lines of zirconium oxide nanoparticle mediated using leaves of Lagerstroemia speciosa, *J. Photochem. Photobiol. B* 169 (2017) 47–55.
[59] R. Govindasamy, M. Govindarasu, S.S. Alharthi, P. Mani, N. Bernaurdshaw, T. Gomathi, M.A. Ansari, M.N. Alomary, B. Atwah, M.S. Malik, V.D. Rajeswari, K. Rekha, S.A. Ahmed, M. Thiruvengadam, Sustainable Green Synthesis of Yttrium Oxide (Y2O3) Nanoparticles Using Lantana Camara Leaf Extracts: Physicochemical Characterization, Photocatalytic Degradation, Antibacterial, and Anticancer Potency, *Nanomaterials (basel)* 12 2393 (2022).
[60] A.H. Idan, A. Al-nayili, N.M.C. Saady, Green synthesis of single phase of ZrO2 nanoparticles via Sonchus asper aqueous extract: antibacterial, antioxidant, cytotoxic, and photocatalytic applications, *Clean Technol: Environ Policy* (2024).
[61] P. Chelliah, S.M. Wabaidur, H.P. Sharma, H.S. Majdi, D.A. Smait, M.A. Najm, A. Iqbal, W.-C. Lai, Photocatalytic Organic Contaminant Degradation of Green Synthesized ZrO2 NPs and Their Antibacterial Activities *Separations* 10 156 (2023).
[62] J.B. Prasanna Kumar, G. Ramgopal, Y.S. Vidya, K.S. Anantharaju, B. Daruka Prasad, S.C. Sharma, S.C. Prashantha, H.P. Nagaswarupa, D. Kavyashree, H. Nagabhushana, Green synthesis of Y2O3:Dy(3+) nanophosphor with enhanced photocatalytic activity, *Spectrochim Acta A Mol. Biomol. Spectrosc.* 149 (2015) 687–697.
[63] S.E. Safitri, Y. Yulizar, Facile green preparation of Y2O3 decorated with ZnFe2O4 using citrus limon (L.) osbeck leaf extract for photocatalytic degradation of malachite green, *Appl. Surf. Sci. Adv.* 21 100589 (2024).
[64] J.B. Prasanna kumar, C. Ramgopal, Y.S. Vidya, K.S. Anantharaju, B. Daruka Prasad, S.C. Sharma, S.C. Prashantha, H.B. Premkumar, H. Nagabhushana, Bio-inspired synthesis of Y2O3: Eu(3+) red nanophosphor for eco-friendly photocatalysis *Spectrochim, Acta A Mol. Biomol. Spectrosc.* 141 (2015) 149–160.
[65] H. Basavanagoudra, V.D. Jangannanavar, M.K. Patil, S.R. Inamdar, K.M. Goudar, Barium oxide nanorods: Catalyst concentration and surface defects' role in degrading methylene blue organic pollutant, *Chem. Phys. Impact* 8 (2024) 100578.
[66] U. Jinendra, D. Bilehal, B.M. Nagabhushana, A.P. Kumar, Adsorptive Removal of Rhodamine B Dye from Aqueous Solution by Using Graphene-Based Nickel Nanocomposite, *Heliyon* 7 (2021) e06851.
[67] A. Das, M.K. Adak, N. Mahata, B. Biswas, Wastewater treatment with the advent of TiO2 endowed photocatalysts and their reaction kinetics with scavenger effect, *J. Mol. Liq.* 338 (2021) 116479.
[68] S. Wu, H. Hu, Y. Lin, J. Zhang, Y.H. Hu, Visible light photocatalytic degradation of tetracycline over TiO2, *Chem. Eng. J.* 382 (2020) 122842.
[69] F. Mukhtar, T. Munawar, K.M. Batoo, H. Khursheed, M.S. Nadeem, S. Hussain, J. Ponraj, M. Koc, F. Iqbal, Oxygen vacancies generation in CeO2 via Y/Nd co-doping with accelerated charge separation by decorating on rGO sheets for sunlight-driven photodegradation of hazardous dyes *Ceram, Int.* 50 (2024) 11486–11499.
[70] T. Munawar, T.S. Alomar, C.-F. Yan, S. Fatima, F. Mukhtar, M.S. Nadeem, N. AlMasoud, S.A. Khan, M. Koc, Y. Zakaria, F. Iqbal, Boosted charge separation via Ce2S3 over dual Z-scheme ZnO-Ce2S3-MnO2 core double-shell nanocomposite for the degradation of diverse dye pollutants *Environ, Res.* 251 (2024) 118675.
[71] T. Munawar, S. Fatima, K.M. Batoo, M.S. Nadeem, F. Mukhtar, S. Hussain, S. A. Khan, M. Koc, F. Iqbal, Enhanced charge carriers separation/transportation via S-scheme ZnCeS–ZnWO heterostructure nanocomposite for photodegradation of synthetic dyes under sunlight *Mater, Chem. Phys.* 314 (2024) 128938.
[72] S. Surendhiran, V. Gowthambabu, A. Balamurugan, M. Sudha, V.B. Senthil Kumar, K.C. Suresh, Rapid green synthesis of CuO nanoparticles and evaluation of its photocatalytic and electrochemical corrosion inhibition performance, *Mater Today* 47 (2021) 1011–1016.
[73] S. Ramamoorthy, S. Surendhiran, D. Senthil Kumar, G. Murugesan, M. Kalaiselvi, S. Kavisree, S. Muthulingam, S. Murugesan, Evaluation of photocatalytic and corrosion properties of green synthesized zinc oxide nanoparticles, J. Mater. Sci.: Mater Electron. 33 (2022) 9722–9731.